

AWARD NUMBER: W81XWH-18-1-0574

TITLE: From Cold to Hot: Leveraging RNA Splicing Therapeutics to Unleash Antitumor Immunity for Breast Cancer Patients

PRINCIPAL INVESTIGATOR: Xiang Zhang

CONTRACTING ORGANIZATION: Baylor College of Medicine  
HOUSTON TX  
77030-3411

REPORT DATE: October 2019

TYPE OF REPORT: Annual

PREPARED FOR: U.S. Army Medical Research and Materiel Command  
Fort Detrick, Maryland 21702-5012

DISTRIBUTION STATEMENT: Approved for Public Release;  
Distribution Unlimited

The views, opinions and/or findings contained in this report are those of the author(s) and should not be construed as an official Department of the Army position, policy or decision unless so designated by other documentation.

# REPORT DOCUMENTATION PAGE

*Form Approved*  
*OMB No. 0704-0188*

Public reporting burden for this collection of information is estimated to average 1 hour per response, including the time for reviewing instructions, searching existing data sources, gathering and maintaining the data needed, and completing and reviewing this collection of information. Send comments regarding this burden estimate or any other aspect of this collection of information, including suggestions for reducing this burden to Department of Defense, Washington Headquarters Services, Directorate for Information Operations and Reports (0704-0188), 1215 Jefferson Davis Highway, Suite 1204, Arlington, VA 22202-4302. Respondents should be aware that notwithstanding any other provision of law, no person shall be subject to any penalty for failing to comply with a collection of information if it does not display a currently valid OMB control number. **PLEASE DO NOT RETURN YOUR FORM TO THE ABOVE ADDRESS.**

<b>1. REPORT DATE</b> Oct 2019			<b>2. REPORT TYPE</b> Annual		<b>3. DATES COVERED</b> 15 Sep 2018-14 Sep 2019	
<b>4. TITLE AND SUBTITLE</b> From Cold to Hot: Leveraging RNA Splicing Therapeutics to  Unleash Antitumor Immunity for Breast Cancer Patients					<b>5a. CONTRACT NUMBER</b>	
					<b>5b. GRANT NUMBER</b> W81XWH-18-1-0574	
					<b>5c. PROGRAM ELEMENT NUMBER</b>	
<b>6. AUTHOR(S)</b> Xiang Zhang  E-Mail: xiangz@bcm.edu					<b>5d. PROJECT NUMBER</b>	
					<b>5e. TASK NUMBER</b>	
					<b>5f. WORK UNIT NUMBER</b>	
<b>7. PERFORMING ORGANIZATION NAME(S) AND ADDRESS(ES)</b>  BAYLOR COLLEGE OF MEDICINE ONE BAYLOR PLAZA HOUSTON TX 77030-3411					<b>8. PERFORMING ORGANIZATION REPORT NUMBER</b>	
<b>9. SPONSORING / MONITORING AGENCY NAME(S) AND ADDRESS(ES)</b>  U.S. Army Medical Research and Materiel Command Fort Detrick, Maryland 21702-5012					<b>10. SPONSOR/MONITOR'S ACRONYM(S)</b>	
					<b>11. SPONSOR/MONITOR'S REPORT NUMBER(S)</b>	
<b>12. DISTRIBUTION / AVAILABILITY STATEMENT</b>  Approved for Public Release; Distribution Unlimited						
<b>13. SUPPLEMENTARY NOTES</b>						
<b>14. ABSTRACT</b> Although immune checkpoint blockade therapy (ICBT) emerged as an effective treatment on a subset of breast cancer patients, it remains a daunting challenge to make more patients respond. Our preliminary studies suggest that inhibition of splicing, a process to join the protein-coding parts of RNAs during gene expression, leads to immunostimulatory responses in triple negative breast cancers (TNBCs). We hypothesized that splicing inhibition accumulates mis-spliced RNAs, which may activate innate immune responses and lead to expression of neo-antigens. In this application, we aim to test this hypothesis and examine if a clinically available splicing inhibitor can synergize with ICBT in immunocompetent models. We will also elucidate specific immune cells that may mediate such synergy.						
<b>15. SUBJECT TERMS</b>						
<b>16. SECURITY CLASSIFICATION OF:</b>				<b>17. LIMITATION OF ABSTRACT</b>	<b>18. NUMBER OF PAGES</b>	<b>19a. NAME OF RESPONSIBLE PERSON</b> USAMRMC
<b>a. REPORT</b>  Unclassified	<b>b. ABSTRACT</b>  Unclassified	<b>c. THIS PAGE</b>  Unclassified	<b>19b. TELEPHONE NUMBER</b> (include area code)			

## Table of Contents

	<u>Page</u>
1. Introduction.....	2
2. Keywords.....	2
3. Accomplishments.....	2
4. Impact.....	5
5. Changes/Problems.....	5
6. Products.....	5
7. Participants & Other Collaborating Organizations.....	5
8. Special Reporting Requirements.....	6
9. Appendices.....	6

## 1. Introduction

This application aims to address the overarching challenges that 1) eliminate the mortality associated with metastatic breast cancer and 2) identify what drives breast cancer growth; determine how to stop it. Escaping immunosurveillance is a prerequisite of tumor growth and metastasis. This application aims to reinvigorated anti-tumor immunity to stop breast cancer growth and eliminate the metastasis.

Immunotherapies, especially immune checkpoint blockade therapies (ICBTs), have achieved remarkable successes in several cancer types including metastatic melanoma and lung cancers, demonstrating the power of anti-tumor immunity when appropriately activated. However, recent clinical trials revealed less impressive efficacies of these treatments in breast cancer, suggesting that ICBTs are not sufficient to activate the immune system. Possible reasons behind this insufficiency include the lack of immune cell cytotoxicity and/or the paucity of neo-antigens. Therapeutic solutions to overcome these roadblocks are urgently needed.

Our previous work has demonstrated an unexpected vulnerability of cancer cells to the perturbation of splicing. Although splicing is almost universally needed for gene expression in all cell types, cancer cells under oncogenic stresses are particularly sensitive to spliceosome inhibition (SI). Our preliminary experiments uncovered that mis-spliced RNAs could accumulate in cytoplasm upon SI, and cause anti-viral responses that are known to further enhance immune cell cytotoxicity. Moreover, proteomic profiling detected peptides resulted from translation of intronic RNAs, which provide a potential source of neo-antigens. Thus, SI appears to be a suitable solution to abovementioned roadblocks of ICBTs.

In this application, we will use a splicing inhibitor with defined pharmacological properties to tackle the hypothesis that SI may convert “cold” tumors to “hot” tumors and enhance ICBT. We will mechanistically investigate how this inhibitor may stimulate innate immune response and enhance immune cell activities using both patient-derived xenograft and genetically engineered mouse models (GEMMs). We will also obtain evidence for activation of antigen-specific adaptive immunity presumably by translation of mis-spliced RNAs. Finally, we will perform proof-of-principle experiments to test if SI sensitizes tumors to ICBT using various syngeneic tumor models. Taken together, these data will likely provide strong rationale for further clinical trials using combined SI and ICBT.

The proposed studies will be jointly carried out by Dr. Thomas Westbrook’s laboratory and Dr. Xiang Zhang’s laboratory. Dr. Westbrook’s group will leverage on their knowledge in splicing and RNA metabolism to investigate tumor-intrinsic signaling pathways that may lead to enhanced innate immune response. Their experience in PDX models will make it possible to establish the connection between splicing and cell-intrinsic innate immune response in human cells. Dr. Zhang’s group will take advantage of their expertise in immune cell profiling to characterize how SI’s impact may extend beyond tumor cells and stimulate the immunity of host. They will also use the GEMMs to functionally study various immune compartments and delineate cellular mechanisms. Taken together, the joint efforts of both groups will powerfully fuel the proposed experiments that span multiple fields.

## 2. Keywords:

Splicing, spliceosome inhibitor, cellular stress, immune-checkpoint blockade therapy, triple negative breast cancer, immune microenvironment.

## 3. Accomplishment

Major Task 1 : Evaluate the activation of tumor innate immune signaling in TNBC PDXs in response to spliceosome inhibition (Month 1-36)

Westbrook Lab.

Major Task 2: Evaluate the activation of tumor innate immune signaling in immunocompetent syngeneic murine TNBC models in response to spliceosome inhibition (Month 1-36)

Westbrook Lab.

Major Task 3 Test whether deficiencies of various host immune cells modulate the efficacy of SI.Tumor models (1-30).

We have been breeding animals as proposed in our application to obtain tumor hosts with specific deficiencies in various lineages of immune cells. The progress has been summarized in the following table.

Model	Targeted cell population	Progress
Cd8 knockout	CD8+ T cells	Successfully bred to C57B/6 and Balb/c background. Tumor transplantation and SI treatment will start as soon as the targeted group size is achieved.
Cd4 knockout	CD4+ T cells	Successfully bred to C57B/6 and Balb/c background. Tumor transplantation and SI treatment will start as soon as the targeted group size is achieved.
Igh-J knockout	B cells	Backcrossing is ongoing...
Fox3P-DTR	T regulatory cells	Mice have been obtained and are being maintained. Backcrossing is ongoing.
Ccr2 knockout	mMDSCs and MΦ	Successfully bred to C57B/6 and Balb/c background. The first in vivo experiments have been performed to examine baseline responses tumors to ICBT in these hosts. In one model (T11), Ccr2 knockout alone led to complete response to ICBT ( <b>Figure 1</b> , below).

As can be seen from above table, the progress is smooth and we do not anticipate significant problem in achieving the proposed goals timely. One interesting finding is that the baseline responses of Ccr2 knockout mice to ICBT in T11 model, a model enriching M2-like macrophages. Specifically, combination of Ccr2 knockout and ICBT appeared to regress T11 tumors completely without recurrences (Figure 1) – indicating a strong role of M2-like macrophages in creating an immunosuppressive microenvironment. This data has been included into our recent publication (attached). Although intriguing and important, this data does exclude the usage of T11 for future SI treatment as the baseline sensitivity to ICBT is already high.

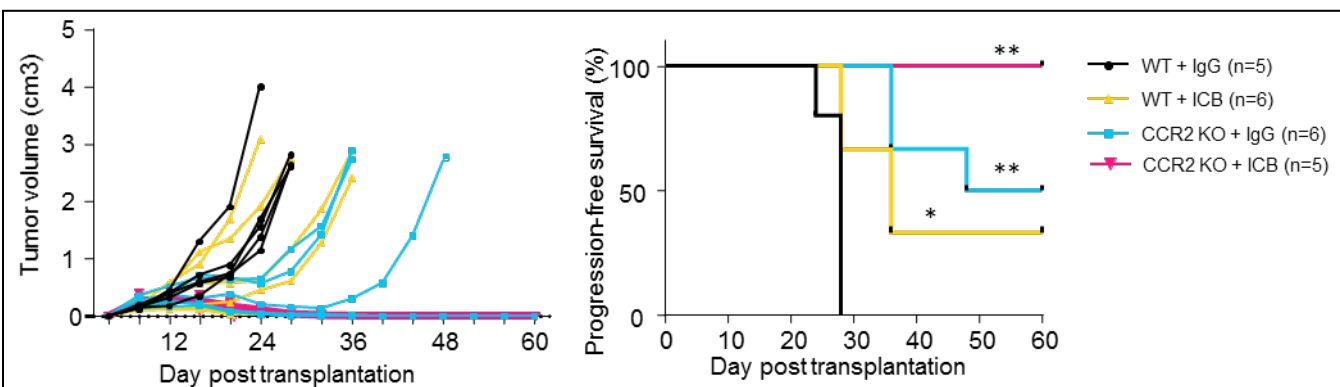
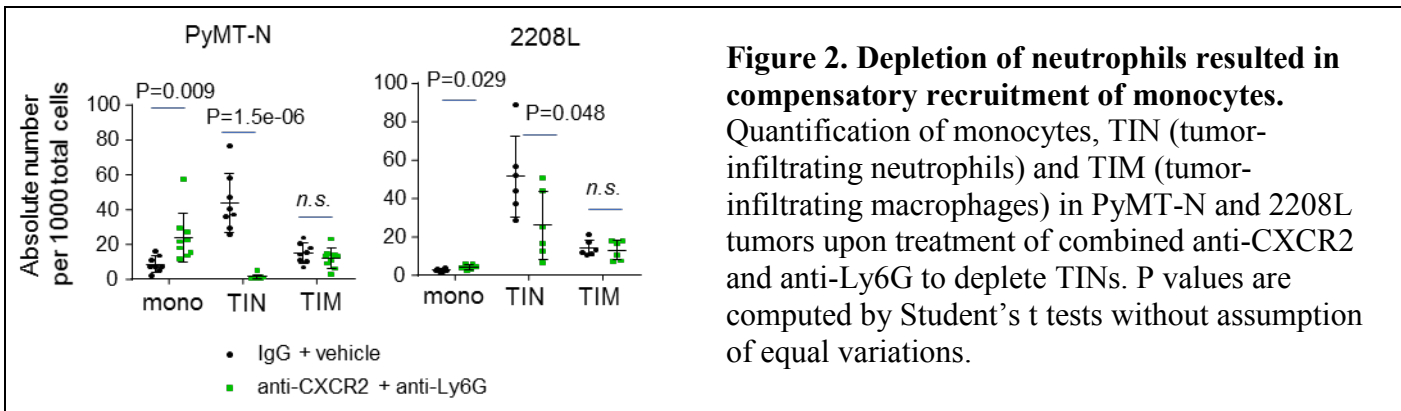


**Figure 1. T11 tumors in CCR2 KO mice exhibited complete response to ICBT.** Left: growth curves of individual T11 tumor in wild type (WT) or CCR2 knockout (CCR2 KO) mice with treatment of ICBT (anti-CTLA4 and anti-PD1) or IgG control. Right: Kaplan-Meier curves show the progression-free survival of animals in the four experimental groups. \* P < 0.05; \*\* P < 0.01. P value was determined by log rank test, comparing each experimental group to WT + IgG control group.

Besides breeding GEMM as host of transplantable tumors, we also proposed to use acute pharmacological treatment to ablate specific immune cell lineages. The proposed experiments and the corresponding progress are shown in the following table.

Treatment	Targeted cell population	Progress
Anti-ASGM1	NK cells	Not started yet.
Csf1R inhibitor	mMDSCs and MΦ	We have performed baseline treatment (without SI) and validated the effects of the drug.
Anti-Ly6G	Granulocytic MDSCs or neutrophils	This experiment has been extensively performed in combination with ICBT. A surprising compensation from monocytes has been observed ( <b>Figure 2</b> ).

We had to combine anti-CXCR2 with anti-Ly6G to achieve a relatively complete depletion of neutrophils. This is consistent with the literature. One noteworthy finding from above experiments is that depletion of neutrophils led to accumulation of monocytes in the tumor microenvironment, which may represent a compensation pathway that maintains immunosuppressive microenvironment. We will follow up with this phenomenon as it might have implications in the proposed SI treatments.



Major Task 4: Test whether the effects of spliceosome inhibition on tumor growth, metastasis, and immune infiltration are through tumor intrinsic signaling. (Month 6-18).

We have successfully obtained tumors expressing drug-insensitive mutant cDNA (SF3B1-R1074H). Drug treatment experiments are ongoing and will be reported after next grant period.

Major Task 5: Identify and characterize the neo-peptidome resulting from translation of intron-retained RNAs in TNBCs treated with spliceosome inhibitor. (Month 12-24).

Samples have been submitted for label free proteomic quantification (LC-MS/MS). Results will be updated in next progress report.

Major Task 6. To determine if specific T cell clones are amplified in tumor-bearing animals – an indication of neo-antigen recognition. (Month 24-36).

Not started yet.

Major Task 7. To determine if spliceosome inhibition potentiates ICBT in multiple syngeneic models. (Month 12-36).

Experiments have been initiated. Results will be updated in next progress report.

#### 4. Impact

Immunotherapies are revolutionizing the treatment of many cancers. Immune checkpoint blockade therapies (ICBT) have been remarkably effective in several cancer types including metastatic melanoma and non-small cell lung cancer. These treatments target negative regulators of the immune system, thereby unleashing anti-tumor immunity. Durable responses are reported in 20-40% of patients with limited toxicity. These successes exemplify the power of the immune system against malignancies. However, ongoing clinical trials suggest that although some breast cancer patients may also benefit remarkably from ICBT, the percentage is disappointingly low as compared to melanoma and lung cancers. In fact, most breast cancers are considered immunologically “cold”, i.e., lacking infiltration of immune cells and not expressing enough proteins that are “foreign” to the immune system.

Mistakes in splicing can result in aberrant RNA sequences. Our preliminary studies indicate that these aberrant RNA sequences may trigger two different responses. First, these RNAs tend to form double-strands, a structure mimics some virus genome. As a result, they can stimulate cells’ defense against virus, which has evolved to cause death of affected cells, and enhance the entire organism’s immune system including T cells and NK cells. Second, some of the aberrant RNAs may be translated into aberrant proteins. Because these proteins are nothing like existing human proteins, they may be recognized as foreign “antigens” and stimulate further immune reactions. Interestingly, both outcomes may be effectively utilized to fight tumors, especially when combined with immunotherapies that require a strong and activated immune system.

Intriguingly, targeting splicing seems to be the exact kind of solution to improve the efficacy of immunotherapy. As mentioned above, it enhances the immune system in general and triggers expression of more foreign proteins. Our preliminary study provides strong evidence supporting this hypothesis. In this application, we will further explore this possibility. Importantly, we will evaluate a clinical grade splicing inhibitor. This inhibitor (H3B-8800) has already been granted orphan drug status in AML/CMML. We will apply this inhibitor to a broad range of patient-derived xenografts (PDXs) and genetically engineered mouse models (GEMMs) in order to drive rational strategies to select TNBC patients who may best respond to the treatment. We will investigate the molecular and cellular mechanisms underlying various models’ responses. We will also test the hypothesis that the inhibition of splicing sensitizes TNBC and may allow more breast cancer patients to benefit from immunotherapies such as ICBT.

Taken together, our proposed research will provide the first broad assessment of this therapeutic approach (targeting RNA splicing) in breast cancer patients. Our goal is to provide a conceptual and pre-clinical framework for initiating clinical trials for breast cancer patients.

#### 5. Changes/Problems

So far, we have not encountered any significant problems or need to change the proposed plans.

#### 6. Products

1. Ik Sun Kim, Yang Gao, Thomas Welte, Hai Wang, Jun Liu, Mahnaz Janghorban, Kuanwei Sheng, Yichi Niu, Amit Goldstein, Na Zhao, Igor Bado, Hin-Ching Lo, Michael J. Toneff, Tuan Nguyen, Wen Bu, Weiyu Jiang, James Arnold, Franklin Gu, Jian He, Deborah Jebakumar, Kimberly Walker, Yi Li, Qianxing Mo, **Thomas F. Westbrook**, Chenghang Zong, Arundhati Rao, Arun Sreekumar, Jeffrey M. Rosen, **Xiang H.-F. Zhang** “Immuno-subtyping of breast cancer reveals distinct myeloid cell biology and immunotherapy resistance mechanisms” Nature Cell Biology, published online August 26, 2019. PMID: PMC6726554

#### 7. Participants & Other Collaborating Organizations

Name:	Weijie Zhang
Project Role:	Postdoctoral Fellow
Researcher Identifier:	N/A

Nearest person month worked	12
Contribution	Dr. Zhang is responsible for all SI-treatment experiments proposed in the application.
Name:	Jun Liu
Project Role:	Research Technician
Researcher Identifier:	N/A
Nearest person month worked	6
Contribution	Ms. Liu is responsible for mouse breeding. She also assists Dr. Zhang in proposed experiments.

Name:	Xiang Zhang
Project Role:	PI/PD
Researcher Identifier:	N/A
Nearest person month worked	1.2
Contribution	Dr. Zhang designed and supervised the experiments described in this report.
Funding Support	Dr. Zhang is also supported by NIH/NCI, Breast Cancer Research Foundation, and McNair Medical Institute.

All collaborators and participants are at Baylor College of Medicine.

### **8. Special Reporting Requirements**

None.

### **9. Appendices**

A copy of the publication on NCB.

# Immuno-subtyping of breast cancer reveals distinct myeloid cell profiles and immunotherapy resistance mechanisms

Ik Sun Kim<sup>1,2,3,4</sup>, Yang Gao<sup>3,4</sup>, Thomas Welte<sup>1,3,4</sup>, Hai Wang<sup>1,3,4</sup>, Jun Liu<sup>1,3,4</sup>, Mahnaz Janghorban<sup>3,4</sup>, Kuanwei Sheng<sup>2,3,5</sup>, Yichi Niu<sup>3,5</sup>, Amit Goldstein<sup>1,3,4</sup>, Na Zhao<sup>3,4</sup>, Igor Bado<sup>1,3,4</sup>, Hin-Ching Lo<sup>1,2,3,4</sup>, Michael J. Toneff<sup>3,4,6</sup>, Tuan Nguyen<sup>3,4,7</sup>, Wen Bu<sup>1,3,4</sup>, Weiyu Jiang<sup>1,3,4</sup>, James Arnold<sup>3,8</sup>, Franklin Gu<sup>3,8</sup>, Jian He<sup>9</sup>, Deborah Jebakumar<sup>9</sup>, Kimberly Walker<sup>6</sup>, Yi Li<sup>1,3,4</sup>, Qianxing Mo<sup>5,10</sup>, Thomas F. Westbrook<sup>3,5,8</sup>, Chenghang Zong<sup>3,5,11</sup>, Arundhati Rao<sup>9</sup>, Arun Sreekumar<sup>3,4</sup>, Jeffrey M. Rosen<sup>3,4</sup> and Xiang H.-F. Zhang<sup>1,3,4,11\*</sup>

**Cancer-induced immune responses affect tumour progression and therapeutic response. In multiple murine models and clinical datasets, we identified large variations of neutrophils and macrophages that define ‘immune subtypes’ of triple-negative breast cancer (TNBC), including neutrophil-enriched (NES) and macrophage-enriched subtypes (MES). Different tumour-intrinsic pathways and mutual regulation between macrophages (or monocytes) and neutrophils contribute to the development of a dichotomous myeloid compartment. MES contains predominantly macrophages that are CCR2-dependent and exhibit variable responses to immune checkpoint blockade (ICB). NES exhibits systemic and local accumulation of immunosuppressive neutrophils (or granulocytic myeloid-derived suppressor cells), is resistant to ICB, and contains a minority of macrophages that seem to be unaffected by CCR2 knockout. A MES-to-NES conversion mediated acquired ICB resistance of initially sensitive MES models. Our results demonstrate diverse myeloid cell frequencies, functionality and potential roles in immunotherapies, and highlight the need to better understand the inter-patient heterogeneity of the myeloid compartment.**

Immune cells participate in every aspect of tumour progression<sup>1</sup>. Many immune cells may play disparate roles—anti-tumorigenic in some situations, pro-tumorigenic in others<sup>2</sup>. For instance, macrophages undergo different activation and polarization<sup>3,4</sup>: the classically activated subsets potentiate anti-tumour immunity<sup>5,6</sup> whereas the alternatively activated subsets promote tumours through multiple mechanisms<sup>7,8</sup>. Neutrophils also play opposing roles in different settings<sup>9–12</sup>, probably due to plasticity and heterogeneity. Therefore, it is critical to understand how immune cell functions vary in different tumour contexts.

Solid tumours also induce systemic immune alterations<sup>13,14</sup>. Immature neutrophils and monocytes may accumulate in blood and immune organs, develop immunosuppressive activity, and alter tumour progression either by infiltrating tumours<sup>11,15</sup> or via homing to distant organs to establish pre-metastatic niches<sup>16–18</sup>.

It remains elusive how these local and systemic immune aberrations are related to inter-tumoural heterogeneity. This has been predominantly characterized based on tumour-intrinsic features<sup>19–21</sup>, where different subtypes of breast cancer exhibit distinct developmental programs, metastatic behaviours and molecular landscapes<sup>22–25</sup>.

Variations in immune profiles have been linked to prognosis, therapeutic responses and breast cancer subtypes<sup>26–30</sup>. However, it remains a challenge to dissect the causal effects and mechanistic functions of different immune cells based solely on clinical data. The current study overcomes these limitations by integrating the immunological characterization of a variety of murine syngeneic mammary tumour models with the analyses of human breast cancer datasets.

## Results

**Immune cell profiling of murine tumour models reveals a dichotomous distribution of macrophages and neutrophils.** We chose eight syngeneic murine tumour models derived from either a BALB/c or C57BL/6 background, and maintained as cell lines or primary tissues (Supplementary Fig. 1a). In particular, PyMT-M and PyMT-N were derived from the same C57/BL6 tumour but exhibited different properties. MMTV-PyMT tumours express oestrogen receptor (ER) in early tumorigenesis, but the tumours progressively lose ER as they develop<sup>31</sup>. We confirmed the lack of ER, progesterone receptor (PR) and ErbB2 expression in PyMT-M and PyMT-N tumours (Supplementary Fig. 1b,c). These and

<sup>1</sup>Lester and Sue Smith Breast Center, Houston, TX, USA. <sup>2</sup>Integrative Molecular and Biomedical Sciences Graduate Program, Houston, TX, USA.

<sup>3</sup>Dan L. Duncan Cancer Center, Houston, TX, USA. <sup>4</sup>Department of Molecular and Cellular Biology, Houston, TX, USA. <sup>5</sup>Department of Molecular

and Human Genetics, Houston, TX, USA. <sup>6</sup>Department of Biology, Widener University, One University Place, Chester, PA, USA. <sup>7</sup>Graduate Program in

Translational Biology and Molecular Medicine, Houston, TX, USA. <sup>8</sup>Verna & Marrs McLean Department of Biochemistry and Molecular Biology, Houston,

TX, USA. <sup>9</sup>Scott and White Medical Center, Baylor Scott and White Healthcare, Temple, Texas, USA. <sup>10</sup>Department of Biostatistics & Bioinformatics, H. Lee

Moffitt Cancer Center & Research Institute, Tampa, FL, USA. <sup>11</sup>McNair Medical Institute Baylor College of Medicine, One Baylor Plaza, Houston, TX, USA.

\*e-mail: [xiangz@bcm.edu](mailto:xiangz@bcm.edu)

previous results<sup>32–34</sup> indicate that, by definition, the eight models represent triple-negative breast cancer (TNBC), which is a heterogeneous group of diseases<sup>21</sup>. Expression of characteristic genes suggested that these models resemble luminal-like (2208L and PyMT-N), basal-like (4T1 and AT3) and the claudin-low (PyMT-M, E0771 and 67NR) subtypes (Supplementary Fig. 1d), covering a spectrum of differentiation<sup>35</sup> and metastatic propensity (Supplementary Fig. 1e). Thus, these models may collectively represent heterogeneous TNBC.

Major immune cell populations were profiled (Supplementary Fig. 1f) when tumours reached a similar size (Supplementary Fig. 1g). Hierarchical clustering was performed to display FACS-determined cell frequencies (Supplementary Fig. 1h). We prioritized different cell types based on inter-model variations and median frequencies (Supplementary Table 1). Tumour-infiltrating neutrophils (TINs) and macrophages (TIMs) were the most frequent and variable cell types across models, as confirmed by immunofluorescence staining of Ly6G and CD68 (Supplementary Fig. 1i).

TINs are defined as CD45<sup>+</sup>CD11b<sup>+</sup>Ly6G<sup>+</sup>Ly6C<sup>med-low</sup> cells, and TIMs are defined as CD45<sup>+</sup>CD11b<sup>+</sup>Ly6G<sup>-</sup>Ly6C<sup>-</sup>F4/80<sup>+</sup> cells (Fig. 1a,b)—note that F4/80<sup>+</sup> cells are CD64<sup>+</sup> (ref. <sup>36</sup>) (Fig. 1c). Wright-Giemsa staining confirmed their polymorphonuclear/multi-lobed and mononuclear morphologies, respectively (Fig. 1d).

We next extended TIM/TIN analyses to an additional seven syngeneic murine and five patient-derived xenograft (PDX) TNBC models. PDXs informed residual immune cells infiltrating human tumours in SCID/Beige mice. Circulating immune cells were examined to evaluate systemic alterations. We performed unsupervised clustering using TIM, TIN, peripheral blood neutrophils (PBNs, CD45<sup>+</sup>CD11b<sup>+</sup>Ly6G<sup>+</sup>Ly6C<sup>med-low</sup>), peripheral blood monocytes (PBMs, CD45<sup>+</sup>CD11b<sup>+</sup>Ly6G<sup>+</sup>Ly6C<sup>high</sup>) and total tumour-infiltrating CD45<sup>+</sup> cells. PBNs and PBMs are potential sources of TINs and TIMs, respectively.

Four clusters were observed (Fig. 1e), driven mainly by the total number of CD45<sup>+</sup> cells and the TIN/TIM ratio (Fig. 1f). PDX tumours in SCID/Beige mice fell mostly into cluster II with low numbers of CD45<sup>+</sup> cells. However, some PDXs were sorted to other clusters, and some murine tumours fell into cluster II and exhibited low T cell infiltration (Supplementary Fig. 1j), arguing against a specific link between immunodeficiency and the ‘cold’ phenotype.

The TIN/TIM ratio is another cluster-driving factor. Clusters I and IV represent tumours with increased TINs, whereas clusters II and III represent those with increased TIMs. The TIN/TIM ratio exhibited a bimodal distribution (Fig. 1f).

The TIN frequency strongly correlated with PBNs (Fig. 1g), indicating that systemic neutrophil accumulation accompanied local TIN enrichment, which was also evidenced by splenomegaly (Supplementary Fig. 1k) and alterations in the bone marrow (Supplementary Fig. 1l). This was opposed to the weak correlations among TIMs, PBMs and tumour-infiltrating monocytes (Fig. 1h,i).

Taken together, we divided pre-clinical models into immunologically cold, macrophage-enriched (MES) or neutrophil-enriched subtypes (NES). MES features local accumulation of macrophages with few neutrophils and little systemic impact. In contrast, NES features local and systemic neutrophil accumulation. In NES, macrophages are still present, sometimes as frequently as neutrophils.

As well as immunosuppressive activities, CD45<sup>+</sup>CD11b<sup>+</sup>Ly6G<sup>+</sup>Ly6C<sup>med-low</sup> cells in tumour-bearing hosts were also defined as granulocytic myeloid-derived suppressor cells (gMDSCs)<sup>15,37</sup>, tumour-associated neutrophils (TANs)<sup>11,37,38</sup> or immunosuppressive neutrophils<sup>39</sup>; CD45<sup>+</sup>CD11b<sup>+</sup>Ly6G<sup>-</sup>Ly6C<sup>high</sup> and CD45<sup>+</sup>CD11b<sup>+</sup>Ly6G<sup>-</sup>Ly6C<sup>-</sup>F4/80<sup>+</sup> cells were also termed monocytic MDSCs<sup>8,15,37</sup> and tumour-associated macrophages<sup>40</sup>, respectively; together these cells were also called immature myeloid cells<sup>41</sup>. However, the suppressive and immature properties of neutrophils and macrophages vary widely among the models in this study. Thus, we prefer the more

generic terms TIN and TIM to describe the comparisons among various models.

**Inter-tumoural variation of neutrophils and macrophages across human TNBCs.** To examine TIM/TIN ratios in human tumours, we first analysed a TNBC dataset with matched tissue microarray (TMA) and NanoString assays of 750 immunity-related genes. Using the human Primary Cell Atlas of BioGPS ([http://biogps.org/dataset/BDS\\_00013/primary-cell-atlas/](http://biogps.org/dataset/BDS_00013/primary-cell-atlas/))<sup>42</sup>, we identified subsets of NanoString genes differentially expressed between macrophages and neutrophils (Fig. 2a). Thirty-three macrophage-specific genes (MSGs) and 45 neutrophil-specific genes (NSGs) were identified to cluster TNBCs (Fig. 2b). Four clusters were uncovered, ranging from MSG-enriched to NSG-enriched (Fig. 2b). One cluster lacks both, and may represent ‘cold’ tumours. The expression of *Elastase* and *G-CSF* genes (both highly relevant for neutrophil biology<sup>43,44</sup>) confirmed the neutrophil variation, and *CD68* expression appears consistent with MSGs (Fig. 2b). Immunohistochemical (IHC) staining of CD68 in matched TMAs revealed variable macrophage infiltration across tumours (Fig. 2b). TMA sections with strong CD68 staining (>10 positive cells) express a higher level of MSGs (Fig. 2c), supporting the NanoString-based analysis. Furthermore, the MSG/NSG ratio exhibited a bimodal distribution (Fig. 2d), consistent with observations in murine models.

Next, we analysed larger datasets using CIBERSORT and TIMER<sup>27,45</sup> to deconvolute immune infiltration from bulk tumour transcriptomes. Hierarchical clustering of TIMER scores of six cell types revealed distinct clusters among the TCGA TNBC dataset (Fig. 2e): a ‘cold’ cluster with overall low immune infiltration, another cluster with higher infiltration of TIM and CD8<sup>+</sup> T cells, and the rest with TIN and other immune cells. In confirmation, we conducted *t*-distributed stochastic neighbour embedding (tSNE) using TIMER scores, resulting in three clusters corresponding to tumours that are cold, TIM-enriched and TIN-enriched (Fig. 2f). Analysis of non-TNBCs in TCGA and TNBC in METABRIC<sup>46</sup> led to similar results (Supplementary Fig. 2a–c). We next analysed CIBERSORT outputs of >1,000 TNBC<sup>47</sup> (Fig. 2g) and observed clusters with heavy neutrophil infiltration (and some macrophages) or tumours enriched with macrophages of various subtypes.

Taken together, using different approaches and patient cohorts, we observed heterogeneous tumour immune microenvironments characterized by the divergent infiltration of neutrophils and macrophages.

### Tumour-intrinsic factors contribute to myeloid cell profiles.

The variations of TIN/TIM frequency within each model are much smaller compared to overall variations across all models (Fig. 3a), suggesting that TIN/TIM frequency is a relatively stable trait. Some other immune cells are also enriched or depleted in specific models (Supplementary Fig. 3a), but exhibited less variation and lower overall frequencies (Supplementary Table 1).

We co-transplanted T11 (MES) and 2208L (NES) tumours into contralateral mammary glands of the same animals (Fig. 3b). This did not alter TIN/TIM frequency (Fig. 3b), further supporting that the TIN/TIM frequency is in part determined by tumour-intrinsic factors. Interestingly, T11 tumours displayed minimal neutrophil infiltration even in the presence of systemic neutrophil accumulation (induced by the contralateral 2208L tumours) (Supplementary Fig. 3b), suggesting an active neutrophil-repelling mechanism.

MMTV-PyMT is an exception: 28 spontaneous tumours derived from 6 animals exhibited diverse TIN/TIM frequency (Fig. 3c). We chose one tumour with intermediate levels of TIN and TIM, and performed animal-to-animal transplantation of small tumour fragments (one per animal). This operation resulted in two primary tumour lines with stable TIN/TIM frequency, named PyMT-M (macrophage-enriched) and PyMT-N (neutrophil-enriched) (Fig. 3c

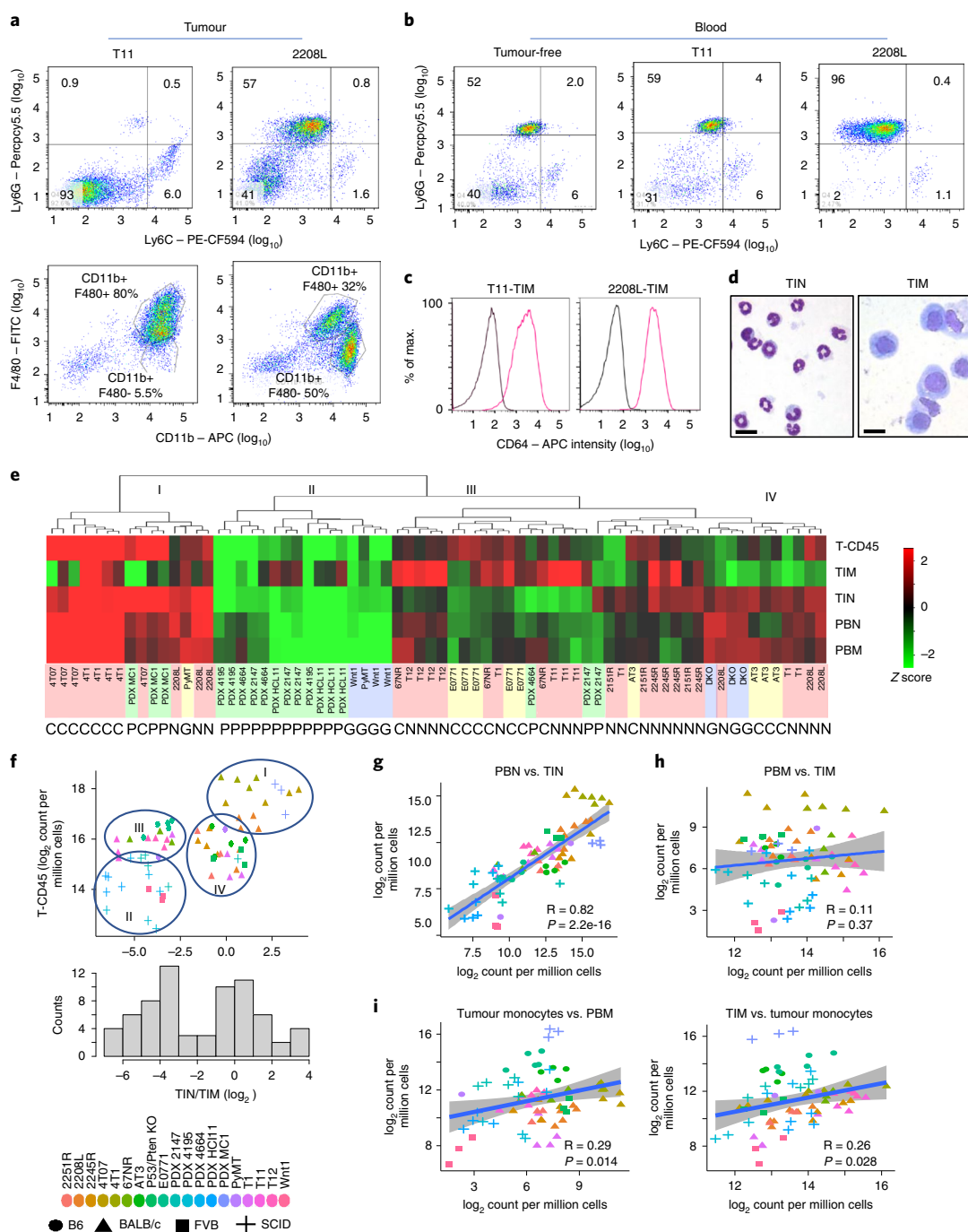


**Fig. 1 | Diverse immune cell profiles in murine mammary tumour models.** **a**, FACS analyses showing dichotomous infiltration of Ly6G<sup>+</sup>Ly6C<sup>med-low</sup> cells (neutrophils) and CD11b<sup>+</sup>F480<sup>+</sup> cells (macrophages) in two representative tumour models. Plots are gated on CD45<sup>+</sup>CD11b<sup>+</sup> cells (top) and CD45<sup>+</sup> cells (bottom). **b**, FACS analyses show variable systemic accumulation of Ly6G<sup>+</sup>Ly6C<sup>med-low</sup> cells (neutrophils) in peripheral blood of tumour-bearing mice. Plots are gated on CD45<sup>+</sup>CD11b<sup>+</sup> cells. For **a, b**, the experiments were repeated at least five times with similar results. **c**, CD64 staining of CD45<sup>+</sup>CD11b<sup>+</sup> Ly6G<sup>+</sup>Ly6C<sup>med-low</sup> F4/80<sup>+</sup> tumour-infiltrating macrophages (TIMs) shows positive signals (pink curve) as compared to the unstained control (black curve) in the T11 and 2208L model. **d**, Wright-Giemsa staining of purified CD45<sup>+</sup>CD11b<sup>+</sup>Ly6G<sup>+</sup>Ly6C<sup>med-low</sup> TINs (left) and CD45<sup>+</sup>CD11b<sup>+</sup>Ly6C<sup>med-low</sup>F4/80<sup>+</sup> TIMs (right). Scale bar, 10  $\mu$ m. For **c, d**, the experiments were done once only. **e**, The heatmap shows unsupervised clustering of 19 breast tumour models ( $n = 70$  biologically independent animals) based on the frequency of total numbers of CD45<sup>+</sup> cells in tumours (T-CD45), TIM, TIN, peripheral blood Ly6C<sup>high</sup> monocytes (PBMs) and peripheral blood neutrophils (PBNs). All cell frequencies are normalized to totals, log-transformed and then z-transformed. The genetic background of each model is encoded by a different colour: pink, BALB/c; blue, FVB; yellow, C57BL/6; green, SCID/Beige. Experimental systems are indicated by letters: C, cell lines; N, p53-null tumour (primary tissue); G, genetically engineered spontaneous tumours; P, PDX models (human tumours in mouse). **f**, Top: scatter plot of total CD45<sup>+</sup> cells against TIN/TIM ratios with the four clusters in **e** indicated by circles. Bottom: histogram of the log<sub>2</sub>-transformed TIN/TIM ratio of the tumour models/biological replicates shown in **e**.  $n = 70$  biologically independent animals. **g-i**, Scatter plots show the correlations among the indicated immune cells. Linear smoothed lines (blue lines) and confidence intervals (grey shade) are shown based on linear regression analyses.  $n = 70$  biologically independent animals. The Pearson correlation coefficients and corresponding  $P$  values are based on two-sided  $t$ -tests. For **f-i**, genetic background and individual tumour models are indicated by distinct point shape and colour, and are shown below **f**.

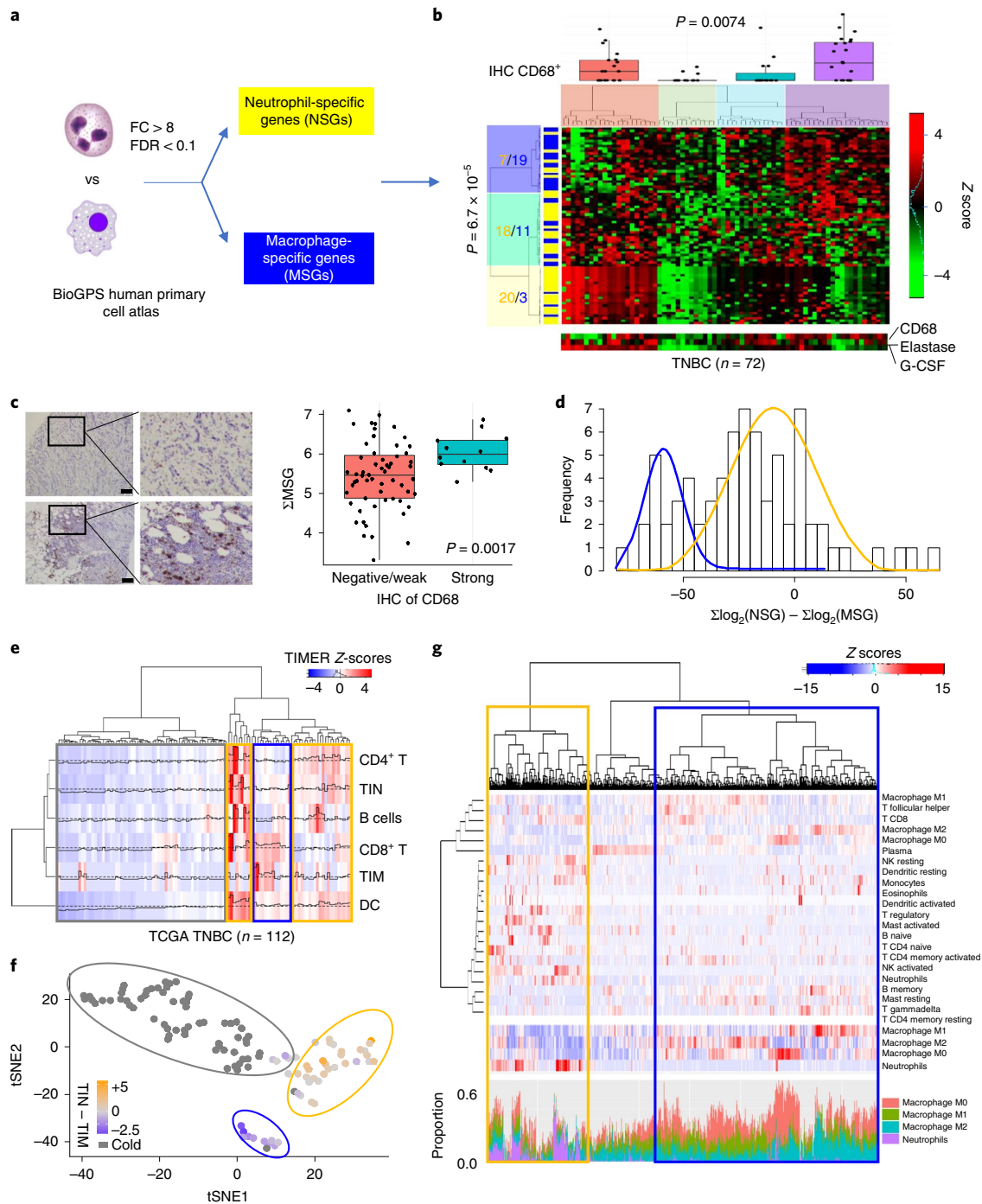


**Fig. 2 | Myeloid cell profiles in human TNBC.** **a**, A schematic showing the derivation of NSGs and MSGs based on the human Primary Cell Atlas of BioGPS. FC, fold change; FDR, false discovery rate. **b**, Unsupervised clustering of a human TNBC NanoString dataset ( $n = 72$  patients) using MSGs (blue) and NSGs (yellow). Boxplots of CD68 IHC quantitation, and the gene expression levels of *CD68*, *Elastase* and *G-CSF* are indicated. The  $P$  value on the row-side was computed by two-sided Fisher's exact test. The  $P$  value along the column side with boxplots was computed based on one-way ANOVA. The colour scale indicates z-scores of  $\log_2$ -transformed, normalized counts. **c**, Left: IHC image of negative/weak (top; representative of 60 patients) or strong (bottom; representative of 12 patients) CD68 staining. Scale bar, 100  $\mu\text{m}$ . Right: boxplots (defined in Methods) show normalized expression of MSG in tumours whose TMA sections exhibit negative or weak CD68 staining (positive cell count  $< 10$ ,  $n = 60$  patients) or strong staining ( $> 10$ ,  $n = 12$  patients). The  $P$  value is computed by two-sided  $t$ -tests with Welch correction. **d**, Histogram of log-transformed ratio of NSG over MSG. The approximated bimodal distribution is shown by solid lines. **e**, Unsupervised clustering of TIMER scores of six indicated immune cells in TNBC of the TCGA dataset ( $n = 112$  patients) after z-transformation. Potential cold, NES and MES clusters are indicated by grey, yellow and blue rectangles, respectively. DC, dendritic cells. **f**, tSNE clustering of the same cohort of tumours ( $n = 112$  patients) as in **e**. Tumours that are 'cold' as determined in **e** are coloured grey. Others are coloured in gradient according to the z-score difference between TIN and TIM. Clusters representing potential NES and MES subtypes are indicated by yellow and blue circles, respectively. **g**, CIBERSORT output of TNBC was obtained from a previous study ( $n = 973$  patients)<sup>47</sup> and reanalysed (top). The contribution of macrophages and neutrophils to the clustering is highlighted in the middle panel. The predicted proportions of neutrophils and macrophages are displayed in stacked bars following the same order. Yellow and blue rectangles indicate clusters of divergent ratios of neutrophils versus macrophages, respectively.

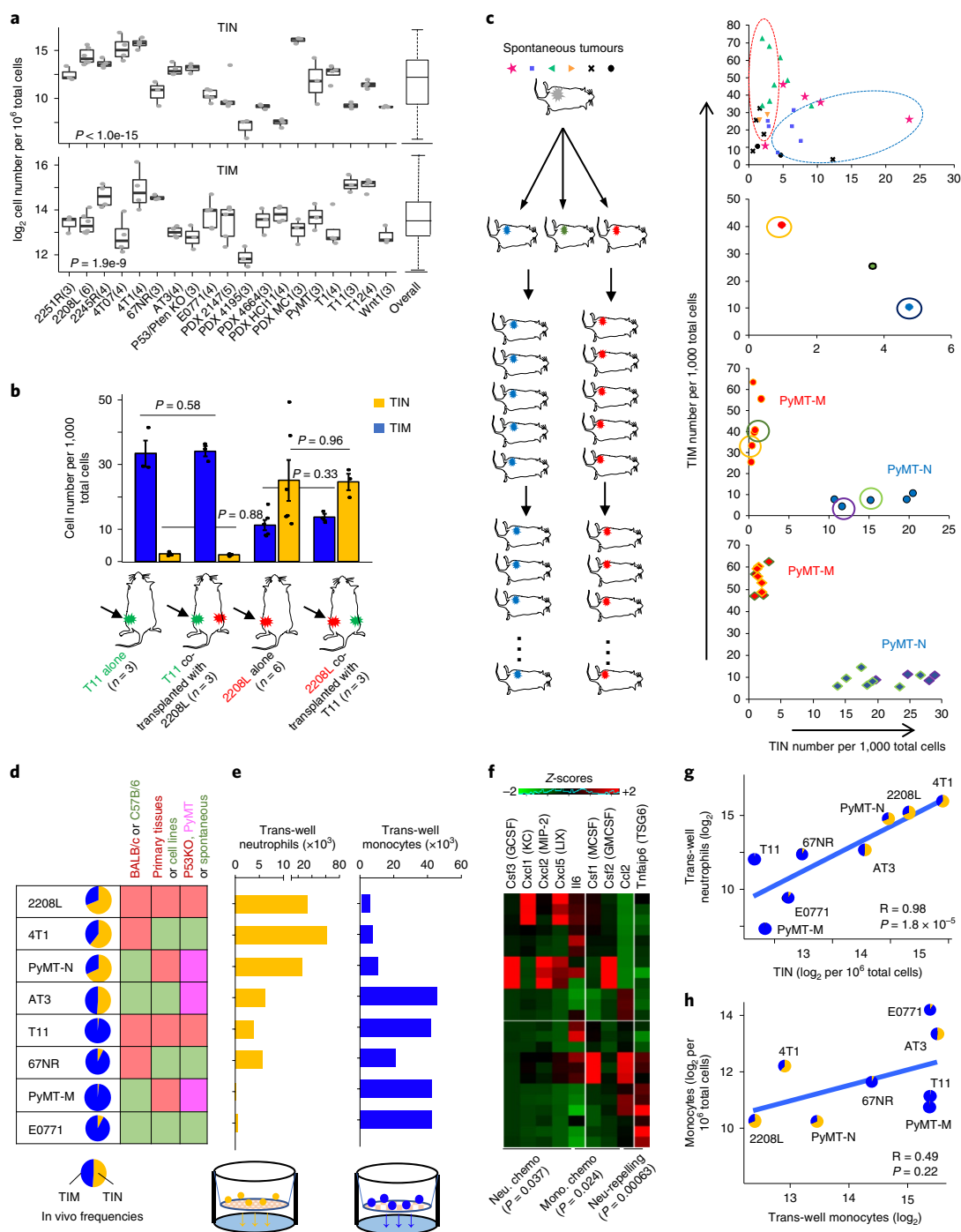


**Fig. 3 | The TIN/TIM frequencies are relatively stable for individual tumour models.** **a**, Boxplots (defined in Methods) of TIN and TIM frequencies (relative to total cells) within individual models and across all models (far right). Each dot represents one tumour from a biologically independent animal, and the sample size of each model is indicated in parentheses. *P* values were computed by one-way ANOVA. **b**, Quantification of TIM and TIN in primary tumours. The sample size of each group is indicated in parentheses. Data are shown as mean  $\pm$  s.d. *P* values were computed by two-sided *t*-tests, not adjusted for multiple comparisons. **c**, Development of MMTV-PyMT sublines that stably maintain divergent myeloid cell profiles. An experimental schematic is shown on the left and quantification of myeloid cells is on the right. Spontaneous tumours risen from the same animal are coded with the same colour and shape. Red or blue dotted circles indicate potential MES or NES tumours, respectively. Tumours used for the next round of transplantation are indicated by solid circles. Points of the resulting tumours are outlined with the same colour as their parental tumour. **d**, TIM/TIN profiles in orthotopic tumours of eight models are presented as pie charts. Other characteristics are shown by colours as indicated by annotations above the table. **e**, Quantification of migrated neutrophils (left) and monocytes (right) towards tumour-conditioned medium. **f**, Heatmap showing the expression level of chemokines and cytokines known to regulate chemotaxis (chemo) of neutrophils and monocytes. Tnfrsf6 is a neutrophil-repelling molecule. Z-scores are based on regularized  $\log_2$ -transformed RNA-seq data. Statistical difference of the sum of each group of genes between NES ( $n = 4$  biologically independent models: 2208L, 4T1, PyMT-N and AT3) and MES ( $n = 4$  biologically independent models: T11, 67NR, PyMT-M and E0771) is assessed by two-sided *t*-tests. **g,h**, Correlation between in vitro migration data and in vivo tumour infiltration data of neutrophils and monocytes ( $n = 8$  biologically independent models). The TIN/TIM profile of each model is indicated as a mini pie chart. Smoothed trend lines are shown. Pearson correlation coefficients and corresponding *P* values (by two-sided *t*-tests) are indicated.

and Supplementary Fig. 3c). Like other NES tumours, PyMT-N induced systemic neutrophil accumulation (Supplementary Fig. 3d). Thus, the original MMTV-PyMT tumour harboured separate TIM- and TIN-enriched regions, which may be explained by the polyclonality of PyMT tumours<sup>48</sup>. Importantly, the TIM/TIN frequencies of transplanted tumours are within the spectrum of spontaneous tumours, suggesting that the MES/NES phenotypes are unlikely to be a result of transplantation-induced inflammation (Fig. 3c). We also compared spontaneous and transplanted MMTV-WNT1 tumours, and observed no significant differences in TIM/TIN frequencies (Supplementary Fig. 3e).

**The frequency of TIN is determined by tumour-derived chemo-attractants.** To investigate whether the TIM/TIN dichotomy in vivo is recapitulated by in vitro chemotaxis of neutrophils or monocytes, we assessed chemo-attraction of bone marrow neutrophils and monocytes by tumour conditioned medium (CM) of the eight models. The variations in chemotaxis (Fig. 3d,e) can be partially explained by expression of chemokines and cytokines known to attract these cells as assessed by RNA-seq (Fig. 3d,f) or qPCR (Supplementary Fig. 3f). In particular, *Tnfrsf6* encodes TSG6, which binds CXCL1/2 and inhibits neutrophil migration<sup>49</sup>. It is expressed in three out of four MES models, and may mediate neutrophil repulsion<sup>49</sup> (Fig. 3b).

Neutrophil migration in vitro tightly correlated with TIN frequency in vivo (Fig. 3g), suggesting that tumour-cell-derived chemokines or cytokines contribute to TIN accumulation. In contrast, monocyte migration only weakly correlated with monocyte frequencies in vivo (Fig. 3h), and did not correlate with TIM frequencies (Supplementary Fig. 3g).

**Alteration of epithelial–mesenchymal transition tilts the TIM/TIM balance.** When cultured in vitro, the eight tumour models exhibited different cell morphologies. Three NES models, 2208L, 4T1 and PyMT-N, were cobblestone/epithelial-like, whereas all MES models were spindle/mesenchymal-like. AT3 was unique: single cells scatter but are not spindle-like (Fig. 4a). Transcriptomic profiling largely confirmed the epithelial and mesenchymal properties, and classified AT3 as mesenchymal (Fig. 4b). Expression of the key genes *Zeb1* and *Cdh1* was validated by qPCR (Supplementary Fig. 4a). Thus, epithelial–mesenchymal transition (EMT) is associated with the TIM/TIN frequency and NES/MES subtyping.

*Zeb1* was upregulated in all mesenchymal lines (Fig. 4b). The reciprocal inhibition between the miR-200 family and *Zeb1* regulates EMT<sup>50–53</sup>. miR-200c expression is higher in epithelial NES tumours (Supplementary Fig. 4b). miR-200c overexpression in MES reduced *Zeb1* (Fig. 4c), shifted cells towards an epithelial phenotype as assessed by an EMT reporter and cell morphology (Supplementary Fig. 4c, d), increased neutrophil-recruiting chemokines including *Cxcl1*, and decreased the neutrophil-repelling molecule *Tnfrsf6* (Fig. 4c). Short hairpin RNA-mediated *Zeb1* knockdown elicited similar changes (Supplementary Fig. 4e). miR-200c expression in human MDA-MB-231 cells also reduced *TNFAIP6* and increased the functional *Cxcl2* homologue *IL8* (Fig. 4c). Consistently, miR-200c overexpression promoted in vitro neutrophil migration in trans-well assays (Fig. 4d), but slightly (statistically significant in one of four models examined) decreased monocyte-related chemokine/cytokine *CCL2* and M-CSF levels (Supplementary Fig. 4f) and corresponding in vitro monocyte migration (Supplementary Fig. 4g). Finally, miR-200c expression in T11 tumours in vivo caused a TIN increase but a TIM decrease (Fig. 4e). Thus, perturbation of EMT reprograms the tumour myeloid microenvironment.

In the TCGA dataset, we used GSEA to identify pathways correlating with TIMER-derived TIM and TIN scores (Fig. 4f). EMT is the top pathway specifically associated with TIM (Supplementary Fig. 4h), supporting our observations in mouse models. The

TIN-associated pathways include PI3K-AKT-mTOR (Supplementary Fig. 4i), consistent with previous findings that the mTOR signalling causes gMDSC accumulation<sup>33</sup>. Gene set variation analysis (GSVA)<sup>54</sup> reinforced the connection between EMT/mTOR pathways and TIM/TIN. Two different EMT signatures<sup>55,56</sup> are associated with the monocyte/macrophage-recruiting cytokines *CSF1* and *CCL2*, the neutrophil-repelling molecule *TS6G* (Fig. 4g) and TIM scores (Supplementary Fig. 4j). The PI3K-AKT-mTOR pathway is associated with the neutrophil-recruiting chemokines *CXCL1* and *IL8*, as well as with TIN scores (Fig. 4g). Finally, miR-200c expression inversely correlated with TIM scores (Fig. 4h). Thus, tumour-intrinsic pathways contribute to the development of a diverse myeloid cell compartment. In particular, EMT may simultaneously drive monocyte/macrophage recruitment and neutrophil exclusion.

**TIMs in MES and NES exhibit different CCR2-dependency and interactions with TINs.** We profiled TIM transcriptomes in four models representative of different genetic backgrounds and immune subtypes. Principle component analysis suggested multi-polar TIM polarization (Fig. 5a). GSVA indicated that T11-TIMs overexpress multiple immunosuppressive hallmark pathways including TGF- $\beta$ , reactive oxygen species (ROS) and mTOR<sup>57,58</sup>, whereas E0771-TIMs overexpress pro-inflammatory pathways including IFN- $\gamma$  and TNF- $\alpha$  (Fig. 5b and Supplementary Fig. 5a). Similar to T11-TIMs, AT3-TIMs overexpress several immunosuppressive pathways such as *Myc* and ROS, but also highly express pro-inflammatory pathways such as TNF- $\alpha$ .

The functional impact of TIMs was evaluated by transplantation of various tumours into CCR2 knockout (CCR2-KO) mice. As expected, Ly6C<sup>high</sup> monocytes were reduced by 3- to 7-fold in all models (Fig. 5c). However, a significant TIM reduction (fold-change >2 and  $P < 0.05$ ) was only seen in MES tumours (Fig. 5c), indicating MES-specific CCR2-dependency. In contrast, NES-TIMs were not affected by CCR2-KO.

The impact of CCR2-KO was heterogeneous on tumour growth (Supplementary Fig. 5b), T cell infiltration (Supplementary Fig. 5c), proliferation, apoptosis or angiogenesis (Supplementary Fig. 5d). Nevertheless, the inverse relationship between TIMs and TINs was evident—that is, whenever TIMs were reduced, TINs increased (Fig. 5c–e). This effect was systemic in animals bearing MES tumours (Supplementary Fig. 5e), but did not occur in tumour-free animals (Supplementary Fig. 5f). Because in two NES models CCR2-KO failed to reduce TIMs, we used combined CSF1-neutralizing antibody (anti-CSF1) and clodrosome to deplete TIMs. This approach can eliminate tissue-resident macrophages, and indeed depleted TIMs in all models tested including NES (Fig. 5f). Interestingly, whereas anti-CSF1 and clodrosome treatment in MES resulted in increased TINs, confirming the CCR2-KO results, it failed to induce a similar increase in NES (Fig. 5f). Thus, the negative impact on TINs appears specific to CCR2-dependent TIMs.

**Neutrophils in NES are immunosuppressive.** TIN transcriptomes of E0771, T11, 2208L and AT3 tumours were also profiled. We used previously identified gene signatures to distinguish normal neutrophils from gMDSCs and/or tumour-associated neutrophils (TANs)<sup>39</sup>. NES-TINs (2208L and AT3) express a substantial proportion of TAN/MDSC genes, whereas MES-TINs (T11 and E0771) are more related to normal neutrophils (Fig. 6a). GSVA of the hallmark pathways further uncovered differences of TINs between NES and MES. The former displayed enhanced expression of several immunosuppressive pathways, including STAT3, TGF- $\beta$  and ROS (Fig. 6b and Supplementary Fig. 6a)<sup>60,61</sup>. In addition, the NOTCH pathway is elevated, supporting a previously reported feedback loop between MDSCs and tumour-initiating cells (Fig. 6b)<sup>33</sup>. A search in additional gene sets revealed adenosine metabolism (Supplementary Fig. 6b) as another immunosuppressive pathway<sup>62,63</sup> upregulated

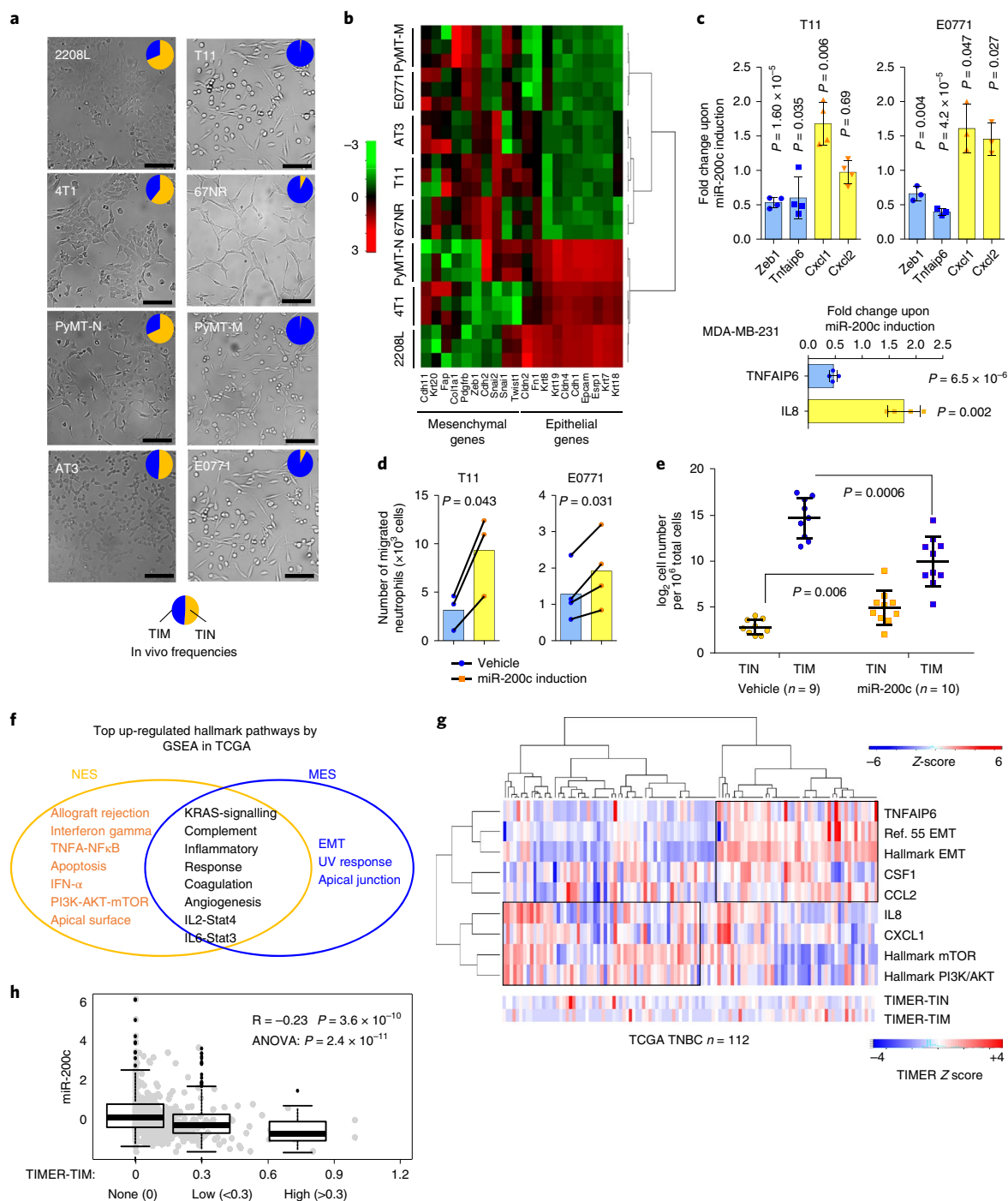


**Fig. 4 | Perturbation of EMT tilts the balance between TIM and TIN.** **a**, Cell morphology of eight tumour models in 2D culture. The pie charts are shown to indicate each model's in vivo TIM/TIN profiles. Scale bars, 100  $\mu$ m. **b**, Heatmap showing the expression level of a panel of EMT-related genes across the eight models (each in technical triplicate). Colour scale indicates z-scores of regularized log-transformed data across columns. **c**, Relative expression of indicated genes in T11 ( $n = 4$ ), E0771 ( $n = 3$ ) and MDA-MB-231 ( $n = 4$ ) models following miR-200c induction with doxycycline. Data are shown as mean  $\pm$  s.d.  $P$  values were determined by two-sided  $t$ -tests. **d**, Quantification of neutrophil migration towards tumour-conditioned medium of T11 ( $n = 3$ ) and E0771 ( $n = 4$ ) cell lines following miR-200c induction with doxycycline. The bar graph represents the mean value of biological replicates.  $P$  values were determined by paired two-sided  $t$ -tests. For **c, d**,  $n$  values indicate numbers of independent experiments. **e**, Quantification of TIM and TIN in orthotopic T11 tumours with or without miR-200c induction. Data are shown as mean  $\pm$  s.d.  $P$  values were determined by two-sided Student's  $t$ -tests. **f**, Venn diagram showing the hallmark pathways associated with TIM and TIN frequencies in the TCGA TNBC dataset ( $n = 112$  patients) gauged by TIMER using GSEA. Significant pathways (FDR  $< 0.05$  empirically determined by random permutations) are shown. **g**, Heatmap showing unsupervised hierarchical clustering of indicated genes and GSEA scores of indicated pathways (in bold) on TNBC of the TCGA dataset. TIMER scores of TIN and TIM are shown on a separate scale after z-transformation. Two EMT-related gene sets (ref.<sup>55</sup> and hallmark EMT) and two mTOR pathway gene sets (hallmark mTOR and hallmark PI3K/AKT) are examined. **h**, Negative correlation between TIMER-TIM scores (TIMER-TIM) and miR-200c expression in the TCGA TNBC dataset ( $n = 112$  patients). Both scatter plots (grey dots) and boxplots (defined in Methods) are shown to treat TIMER-TIM as continuous and categorical variables (cutoffs indicated), respectively. A two-sided  $t$ -test (for the Pearson correlation coefficient) and one-way ANOVA are applied to compute  $P$  values.

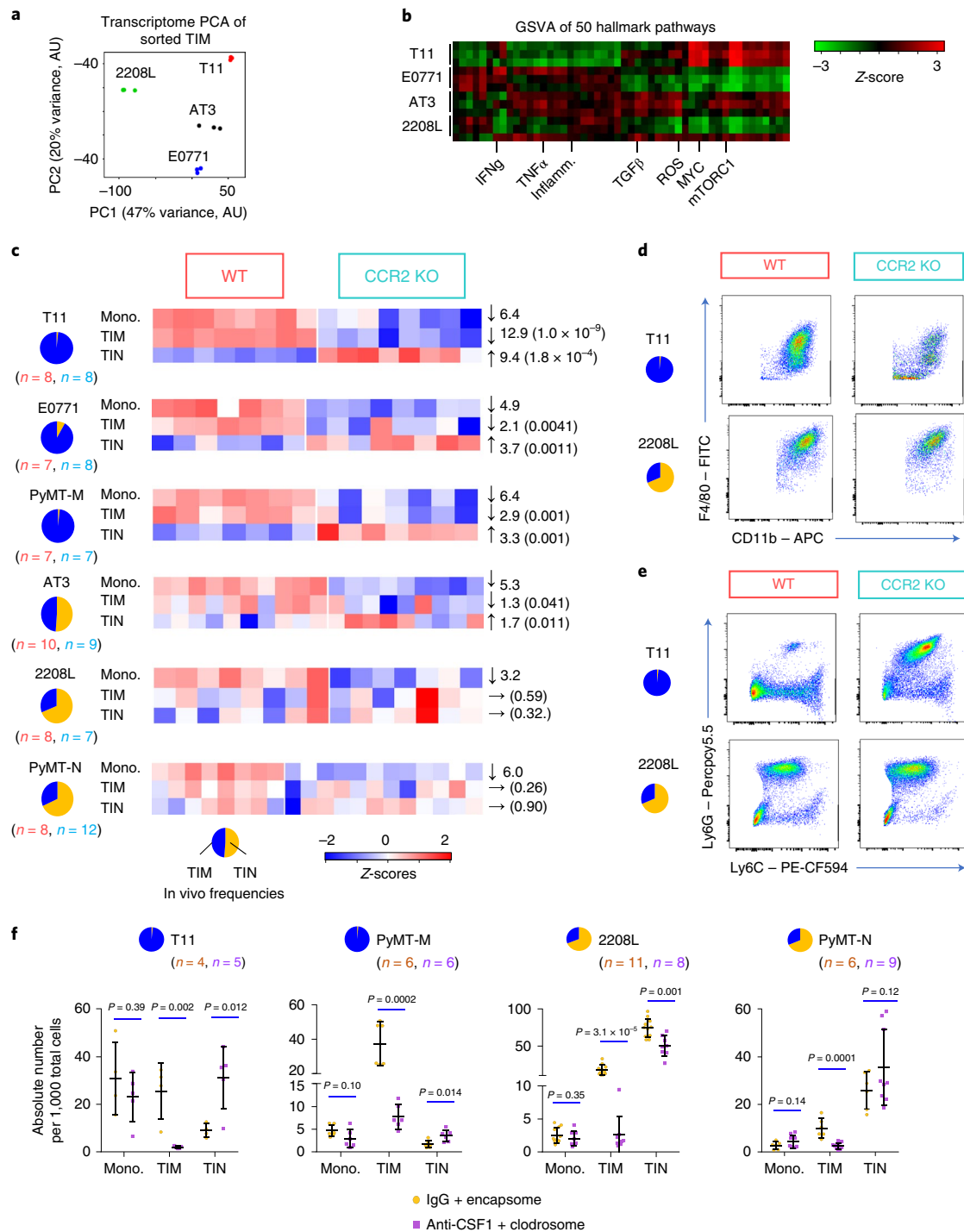


**Fig. 5 | Inter-tumoural heterogeneity of TIMs and inverse change of TINs following TIM depletion.** **a**, Principle component analysis (PCA) of TIMs of four tumour models ( $n=3$  biologically independent samples for each model). **b**, Heatmap shows unsupervised clustering of TIMs purified from four tumour models ( $n=3$  biologically independent samples for each model) using GSEA of the 50 hallmark pathways from MSigDB. Pathways related to immunosuppressive or immunostimulatory activities are shown. The heatmap with complete pathway annotations is shown in Supplementary Fig. 5a. **c**, Heatmaps showing the impact of CCR2-KO-mediated Ly6C<sup>high</sup> monocyte depletion on the frequency of TIM and TIN in the indicated tumour models. Numbers in parentheses show the specific  $n$  values of biologically independent mice per group denoted by different colours. The absolute cell numbers were quantified by flow cytometry. Arrows to the right of the heatmaps show the direction of changes. Numbers beside the arrows indicate fold changes of immune cell infiltration in CCR2-KO compared to WT. Numbers in parentheses indicate  $P$  values computed by two-sided  $t$ -tests. **d**, Example FACS plots showing the alteration of TIMs (CD11b<sup>+</sup>Ly6C<sup>+</sup>Ly6C<sup>+</sup>F4/80<sup>+</sup>) in WT and CCR2-KO hosts bearing T11 and 2208L tumours as representatives of MES and NES, respectively. **e**, Example FACS plots showing the alteration of TINs (CD11b<sup>+</sup>Ly6G<sup>+</sup>Ly6C<sup>med-low</sup>) in WT and CCR2-KO hosts bearing T11 and 2208L tumours as representatives of MES and NES, respectively. For **d,e**, the results are representative of at least eight biologically independent animals. **f**, Quantification of tumour-infiltrating monocytes, TIM and TIN in the indicated tumour models following treatment of anti-CSF1 and clodrosome. Numbers in parentheses show the specific  $n$  values of biologically independent mice per group denoted by different colours. Data are shown as mean  $\pm$  s.d.  $P$  values were determined by two-sided  $t$ -tests.

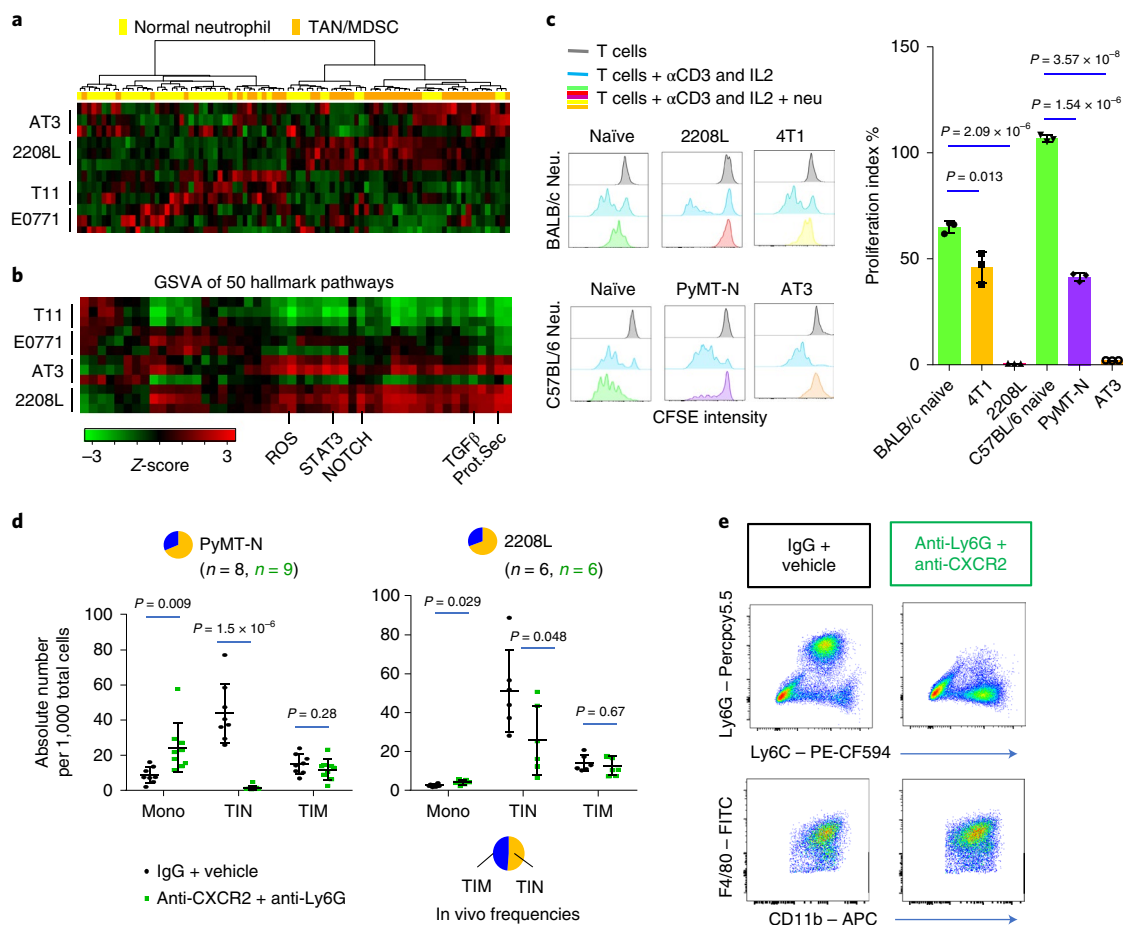


**Fig. 6 | TINs in NES tumours express multiple immunosuppressive pathways, and negatively regulate Ly6C<sup>+</sup> monocyte recruitment.** **a**, Heatmap showing unsupervised hierarchical clustering of TINs purified from four tumour models ( $n=3$  biologically independent samples for each model) using gene characteristic of normal neutrophils or TANs and/or MDSCs as published previously<sup>59</sup>. **b**, Heatmap showing unsupervised clustering of TINs of four tumour models ( $n=3$  biologically independent samples for each model) using GSEA of the 50 hallmark pathways from MSigDB. Pathways related to immunosuppressive activities are shown. The heatmap with all pathways annotated is shown in Supplementary Fig. 6a. **c**, In vitro immunosuppression assay by co-culturing bone marrow neutrophils from indicated NES-tumour-bearing animals and splenic T cells. Proliferation of T cells was determined based on CFSE intensity as measured by FACS. A left-shift of CFSE intensity histogram indicates dilution of signals by proliferation. Data are shown as mean  $\pm$  s.d. of three biological replicates (neutrophils from three different mice).  $P$  values were determined by two-sided  $t$ -tests. **d**, Quantification of monocytes, TIM and TIM in NES tumours (PyMT-N and 2208L) following treatment of anti-CXCR2 and anti-Ly6G. Numbers in parentheses show the specific  $n$  values of biologically independent mice per group denoted by different colours. Data are shown as mean  $\pm$  s.d.  $P$  values were computed by two-sided Student's  $t$ -tests. **e**, Example FACS plots showing the alteration of TIMs (CD11b<sup>+</sup>Ly6G<sup>+</sup>Ly6C<sup>med-low</sup>), monocytes (CD11b<sup>+</sup>Ly6G<sup>+</sup>Ly6C<sup>+</sup>), TIMs (CD11b<sup>+</sup>Ly6G<sup>+</sup>Ly6C<sup>-</sup>F4/80<sup>+</sup>) in hosts bearing PyMT-N tumours (NES) treated with anti-Ly6G and anti-CXCR2, or IgG control. The results are representative of at least five biologically independent animals.

in NES-TINs. CD11b<sup>+</sup>Ly6G<sup>+</sup> cells in the bone marrow of NES-tumour-bearing animals suppressed T cell proliferation in vitro (Fig. 6c), thereby meeting the definition of gMDSCs<sup>37,64</sup>. Thus, TINs in different immune subtypes differ in both frequency and immunosuppressive activity. Moreover, NES tumours induce systemic accumulation of gMDSCs.

Given the negative impact of TIMs on TINs recruitment in MES, we asked if a reciprocal regulation occurs in NES. By applying anti-CXCR2 and anti-Ly6G, we reduced NES-TINs by 2- to 10-fold. This resulted in an increase of Ly6C<sup>+</sup> monocytes but not TIMs (Fig. 6d,e), suggesting a negative regulation of TIM on monocyte recruitment. The increased monocytes did not differentiate into TIMs. In contrast, monocytes in MES readily differentiate into TIMs (Fig. 5c). Thus, the definition of MES includes tumours enriched with TIMs and their precursor monocytes.

**NES and MES respond differently to immune checkpoint blockade.** We subjected eight models (4 NES, 3 MES, and MMTV-WNT1

as a representative of a 'cold' tumour) to immune checkpoint blockade (ICB) therapy (anti-PD1 and anti-CTLA4). The NES and cold tumour did not respond (Fig. 7a), even when the dosage was escalated to the maximum tolerable level (Supplementary Fig. 7a). MES showed largely variable responses (Fig. 7a and Supplementary Fig. 7a). We also observed that MES-tumour-derived cell lines (for example, PyMT-M), when transplanted, gave rise to tumours exhibiting stronger ICB responses than tumours derived from tissue fragments of the same model (Fig. 7a and Supplementary Fig. 7b). However, NES-derived cell lines (for example, PyMT-N) remained resistant (Supplementary Fig. 7b). TINs may create an immunosuppressive microenvironment independent of checkpoints, rendering these tumours non-responsive to ICB. ICB responses do not correlate with baseline tumour-infiltrating CD8<sup>+</sup> T cells (Supplementary Fig. 7c) or PDL1 expression (Supplementary Fig. 7d). However, MES, but not NES, exhibited increased CD8<sup>+</sup> T cell infiltration post-treatment, and sometimes a reduction of the percentage of PD1<sup>+</sup> T cells (Supplementary Fig. 7e), suggesting that ICB restores CD8<sup>+</sup> T cell activity in MES.

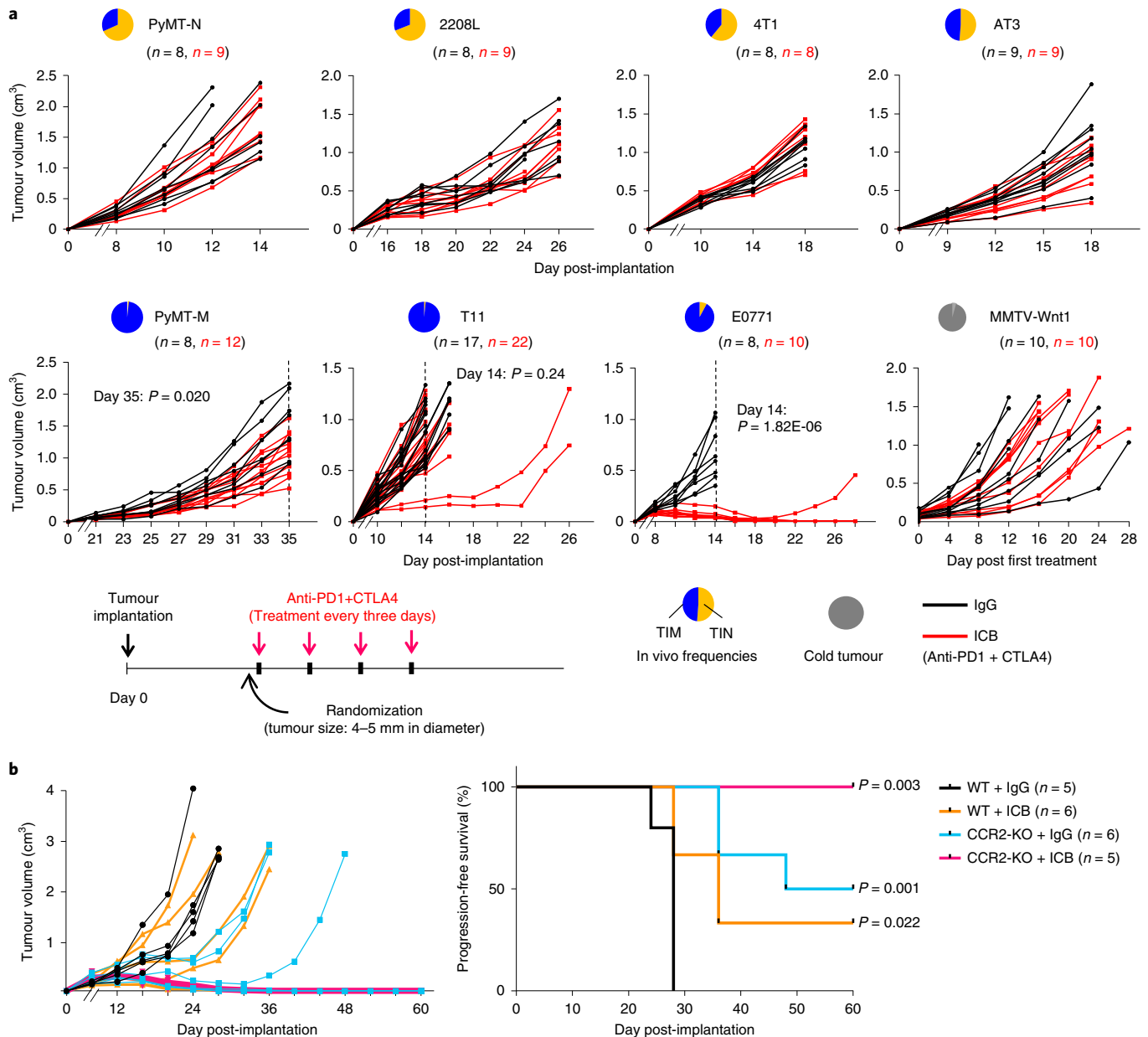


**Fig. 7 | Heightened accumulation of immunosuppressive TIMs or gMDSCs is associated with de novo resistance to ICB.** **a**, Tumour growth curves show responses of indicated tumour models to ICB therapy (anti-PD1 and anti-CTLA4). A treatment schematic is shown below the growth curves. Numbers in parentheses show the specific  $n$  values of biologically independent mice per group denoted by different colours. Dotted lines indicate the time point at which tumour sizes were compared between control and treatment groups.  $P$  values were computed by two-sided  $t$ -test. **b**, Left: growth curves of T11 tumour in WT or CCR2-KO mice with or without treatment of ICB (anti-PD1 and anti-CTLA4). Right: Kaplan–Meier curves show the progression-free survival of the animals in four groups. Numbers in parentheses show the specific  $n$  values of biologically independent mice.  $P$  values were determined by two-sided log rank test, comparing each experimental group to WT and IgG control group.

Although MES exhibited better responses than NES, the extent varied. T11 is enriched with immunosuppressive TIMs (Fig. 5b), and CCR2-KO improved ICB responses: 5/5 T11 tumours regressed completely (Fig. 7b). The same treatment in E0771 and PyMT-M did not significantly alter responses (Supplementary Fig. 7f).

We wanted to know if immunosuppressive TIMs mediate de novo ICB resistance. TIM reduction by combined anti-CXCR2 and anti-Ly6G treatment did not lead to improved ICB responses in NES (Supplementary Fig. 7g), perhaps due to the compensatory increase of immunosuppressive monocytes (Fig. 6d), as indicated by T cell proliferation assay (Supplementary Fig. 7h). ICB resistance

was confirmed by lack of alterations in T cell frequencies or PD1<sup>+</sup> proportion (Supplementary Fig. 7i).

**MES accumulates immunosuppressive TIMs when acquiring resistance to ICB.** E0771 tumours (>90%) exhibited durable responses to ICB, even after treatment cessation. One tumour recurred with increased TIMs, which was designated E0771-ICBR. When further transplanted, neutrophil accumulation persisted both locally and systemically (Fig. 8a). Moreover, E0771-ICBR expresses higher levels of *Cxcl1* and lower levels of *Tnfrsf6* (Fig. 8b). Neutrophils from E0771-ICBR-bearing animals potently

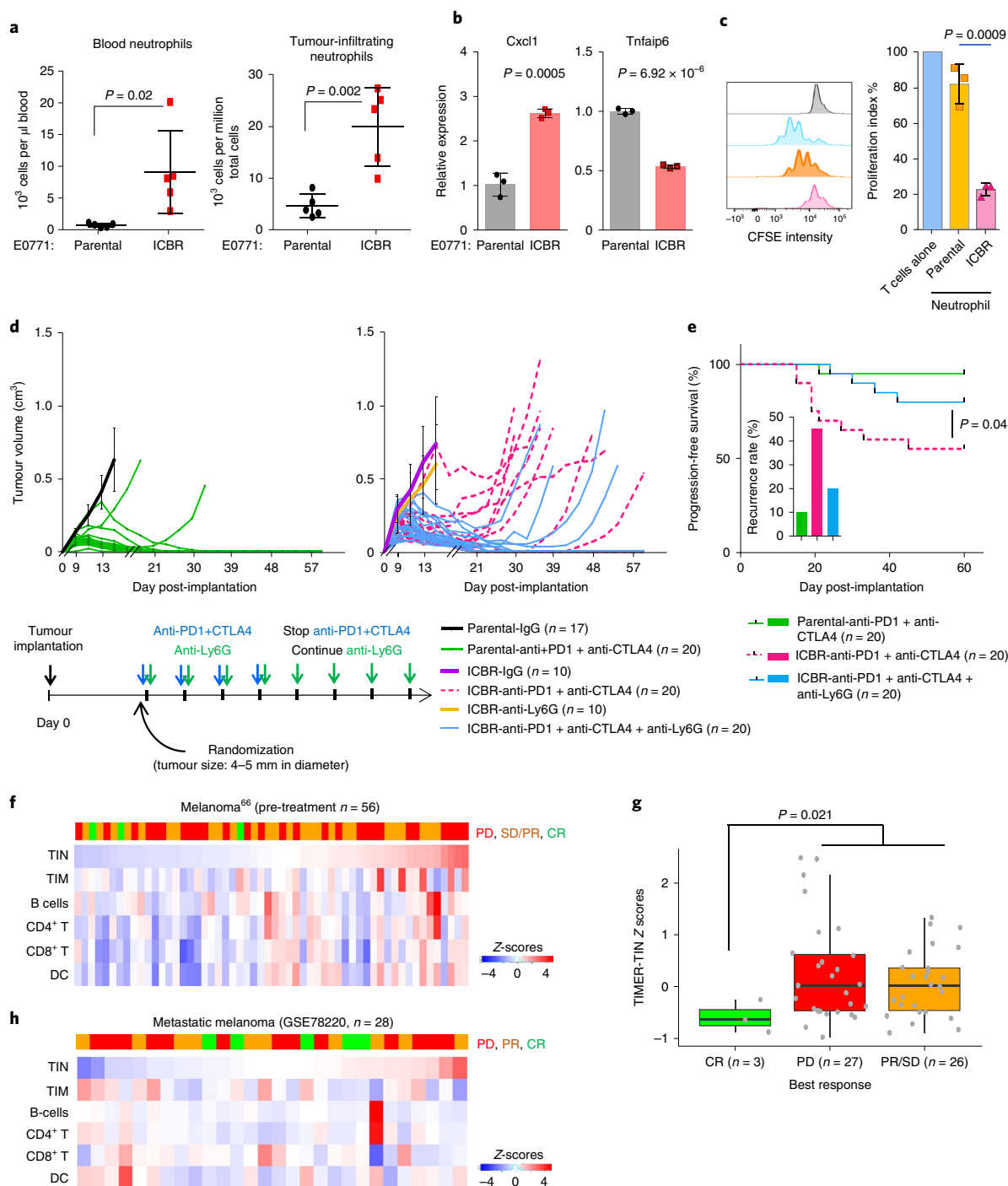


**Fig. 8 | TINs mediate acquired resistance to ICB.** **a**, Quantification of peripheral blood neutrophils and TINs in animals transplanted with parental ( $n=5$ ) or recurrent (ICBR,  $n=5$ ) E0771 tumours. Data are shown as mean  $\pm$  s.d.  $P$  values were determined by a two-sided  $t$ -test. **b**, Relative expression of the indicated genes in parental ( $n=3$ ) and ICBR ( $n=3$ ) E0771 cell lines. Data are shown as mean  $\pm$  s.d.  $P$  values were determined by a two-sided  $t$ -test. **c**, An *in vitro* immunosuppression assay was performed by co-culturing bone marrow neutrophils from parental and ICBR E0771 tumour-bearing animals and splenic T cells. T cell proliferation was determined using CFSE intensity as measured by FACS. Data are shown as mean  $\pm$  s.d. of three biological replicates (neutrophils from three different mice).  $P$  values were computed using two-sided  $t$ -tests. **d**, Therapeutic responses of parental and ICBR E0771 tumours to ICB (anti-PD1 and anti-CTLA4) and/or neutrophil depletion (anti-Ly6G). A treatment schematic is shown below the growth curves. Recurrence rate post-ICB is shown on the right. Because experimental groups without ICB never regressed (parental IgG, ICBR IgG and ICBR anti-Ly6G), they were not further analysed for recurrence rate or progression-free survival. The sample size of each group is provided in parentheses. Growth curves of parental IgG, ICBR IgG and ICBR anti-Ly6G groups are homogeneous, and therefore are summarized as mean  $\pm$  s.d. at each time point. **e**, Kaplan–Meier curves show the progression-free survival of parental or ICBR E0771 tumour-bearing animals subjected to either ICB alone or ICB and anti-Ly6G.  $P$  values were determined by two-sided log likelihood test. Recurrence rate post-ICB is shown as bar graphs under the curves. **f**, Heatmap showing the TIMER scores of indicated immune cells in a metastatic melanoma dataset<sup>66</sup>. Red, orange and green bars indicate progressive diseases (PD), partial response (including stabilized diseases, PR/SD) and complete response (CR), respectively. **g**, Boxplots (defined in Methods) of TIMER-TIN scores in patients with different responses to nivolumab. The sample size of each group is indicated in parentheses.  $P$  values were determined by two-sided  $t$ -test. **h**, The same as **f** except for a different metastatic melanoma dataset<sup>67</sup>.

suppressed T cell proliferation, displaying features of gMDSC (Fig. 8c), and were Ly6G<sup>low</sup> (Supplementary Fig. 8a), representing immature neutrophils<sup>39,65</sup>. The recurrent tumours accumulated neutrophils in the bone marrow (Supplementary Fig. 8b,c) and led to splenomegaly (Supplementary Fig. 8d). These alterations mirrored NES, and suggest an MES-to-NES switch following acquisition of ICB resistance. Combination of anti-Ly6G and ICB reduced recurrence by 50% and significantly improved progression-free survival of the tumour-bearing animals (Fig. 8d,e).

Similar results were obtained in PyMT-M. Cell-line-derived PyMT-M tumours exhibited tumour stasis or regression following ICB (Supplementary Fig. 7b). A recurrent derivative (PyMT-M-ICBR) showed significantly increased accumulation of TINs locally and systemically (Supplementary Fig. 8e). *Cxcl1/2* expression was increased, whereas *Tnfrsf6* expression was decreased (Supplementary Fig. 8f).

Thus, accumulation of immunosuppressive TINs or gMDSCs is associated with acquired ICB resistance in MES, and targeting these cells may alleviate resistance to ICB.

**Exceptional neutrophil accumulation is associated with poor patient outcome.** We used published metastatic melanoma datasets to query TIN roles in ICB response in human tumours, as relevant datasets are not yet available for TNBC. TIMER was applied to predict immune cell infiltration (Fig. 8f,h). In one dataset (Fig. 8f)<sup>66</sup>, TIN scores were significantly higher in patients with progressive disease (PD) or partial response (SD/PR) than in those exhibiting a complete response (CR) (Fig. 8g). In another dataset<sup>67</sup>, 70% of patients with PD were either top- or bottom-ranked according to the TIN score (Fig. 8h). We observed a significant inverse correlation between TIM and TIN scores ( $R = -0.53$ ,  $P = 0.0033$ ). Low-TIN tumours might enrich TIMs that attenuate ICB efficacy, similarly to T11 (Fig. 7b). Normality tests revealed 20% of tumours beyond a normal distribution, representing a distinct TIN-enriched group (Supplementary Fig. 8g,h). Applying the 20% cutoff and combining both datasets, we found a PR depletion and PD enrichment in NES-like melanoma (Supplementary Fig. 8i), supporting the correlation between heightened neutrophil accumulation and ICB resistance.

## Discussion

One possible limitation of our study is the usage of transplantable tumours (cell lines or primary tissues). Tissue injury during transplantation and the absence of natural tumorigenesis may influence immune cell profiles. In two models, we compared spontaneous tumours with their transplantable derivatives, and found no significant difference in TIM/TIN frequency (Fig. 3c and Supplementary Fig. 3e). Genetically engineered models with spontaneous tumours also have caveats. Thus, it is important to compare the immune landscape of pre-clinical models to human tumours, and ideally at a single-cell level.

Different immune subtypes may co-exist intra-tumourally as demonstrated in PyMT. NES and MES tumours can be co-transplanted to a single host without affecting one another. This mutual exclusivity may result from the strong attraction of neutrophils in NES, whereas MES seems to repel neutrophils through EMT-mediated inhibition of neutrophil chemotaxis. Furthermore, neutrophils and monocytes/macrophages appear to negatively regulate each other, consistent with a previous report<sup>68</sup>. These mechanisms may cause spatial segregation between MES and NES within the same tumour.

Our data suggest different TIM biology between MES and NES tumours. In MES, TIMs are derived from CCR2<sup>+</sup> monocytes, they may be polarized to M1-like or M2-like, and they negatively regulate TIN recruitment. In NES, TIMs are not clearly M1-M2 polarized, they are not impacted by CCR2-KO, nor do they regulate TINs. These observations suggest a more complicated biology of

NES-TIMs, perhaps involving different cells of origin, differentiation, proliferation or activation.

NES tumours drive systemic gMDSC accumulation. However, MES-TINs are more similar to normal neutrophils, and might even perform anti-tumorigenic functions as previously shown<sup>9</sup>. Thus, the functions of TINs are determined by the entire myeloid compartment, further highlighting the importance of investigating the interactions among multiple cell types.

Previous studies linked EMT to immunosuppression, as EMT upregulates checkpoint molecules in cancer cells<sup>69,70</sup>. Here, we show that reversion of EMT may be accompanied by an influx of neutrophils, thereby switching the source of immunosuppression to neutrophils.

A recent study suggested that loss of p53 dictates systemic accumulation of pro-metastasis neutrophils in breast cancer<sup>71</sup>. One of our models (T11) lacks p53 but did not induce neutrophil accumulation, indicating more complicated mechanisms. The present study and a previous study from our laboratories<sup>33</sup> suggest that additional tumour-intrinsic pathways (e.g., EMT and mTOR) and interplay between different immune cell populations (e.g., neutrophils and macrophages) need to be considered.

Overall, our studies highlight systematical characterization of microenvironmental heterogeneity by integrating multiple cell types in multiple tumour models, and show that the heterogeneity of breast cancer extends to the immune microenvironment. Therefore, in addition to mutation load and antigenicity, the tumour myeloid compartment should be examined to tailor immunotherapies.

## Online content

Any methods, additional references, Nature Research reporting summaries, source data, statements of code and data availability and associated accession codes are available at <https://doi.org/10.1038/s41556-019-0373-7>.

Received: 30 June 2018; Accepted: 4 July 2019;

Published online: 26 August 2019

## References

- Joyce, J. A. & Pollard, J. W. Microenvironmental regulation of metastasis. *Nat. Rev. Cancer* **9**, 239–252 (2009).
- Kim, I. S. & Zhang, X. H. F. One microenvironment does not fit all: heterogeneity beyond cancer cells. *Cancer Metas. Rev.* **35**, 601–629 (2016).
- Porta, C. et al. Macrophages in cancer and infectious diseases: the 'good' and the 'bad'. *Immunotherapy* **3**, 1185–1202 (2011).
- Mantovani, A., Sica, A. & Locati, M. Macrophage polarization comes of age. *Immunity* **23**, 344–346 (2005).
- Schreiber, R. D., Old, L. J. & Smyth, M. J. Cancer immunoeediting: integrating immunity's roles in cancer suppression and promotion. *Science* **331**, 1565–1570 (2011).
- Pyonteck, S. M. et al. CSF-1R inhibition alters macrophage polarization and blocks glioma progression. *Nat. Med.* **19**, 1264–1272 (2013).
- Qian, B. Z. & Pollard, J. W. Macrophage diversity enhances tumor progression and metastasis. *Cell* **141**, 39–51 (2010).
- Gallina, G. et al. Tumors induce a subset of inflammatory monocytes with immunosuppressive activity on CD8<sup>+</sup> T cells. *J. Clin. Invest.* **116**, 2777–2790 (2006).
- Granot, Z. et al. Tumor entrained neutrophils inhibit seeding in the premetastatic lung. *Cancer Cell* **20**, 300–314 (2011).
- Wculek, S. K. & Malanchi, I. Neutrophils support lung colonization of metastasis-initiating breast cancer cells. *Nature* **528**, 413–417 (2015).
- Fridlender, Z. G. et al. Polarization of tumor-associated neutrophil phenotype by TGF-beta: 'N1' versus 'N2' TAN. *Cancer Cell* **16**, 183–194 (2009).
- Park, J. et al. Cancer cells induce metastasis-supporting neutrophil extracellular DNA traps. *Sci. Transl. Med.* **8**, 361ra138–361ra138 (2016).
- Redig, A. J. & McAllister, S. S. Breast cancer as a systemic disease: a view of metastasis. *J. Int. Med.* **274**, 113–126 (2013).
- Egeblad, M., Nakasone, E. S. & Werb, Z. Tumors as organs: complex tissues that interface with the entire organism. *Dev. Cell* **18**, 884–901 (2010).
- Gabrilovich, D. I. & Nagaraj, S. Myeloid-derived suppressor cells as regulators of the immune system. *Nat. Rev. Immunol.* **9**, 162–174 (2009).
- Kaplan, R. N. et al. VEGFR1-positive haematopoietic bone marrow progenitors initiate the pre-metastatic niche. *Nature* **438**, 820–827 (2005).

17. Catena, R. et al. Bone marrow-derived Gr1+ cells can generate a metastasis-resistant microenvironment via induced secretion of thrombospondin-1. *Cancer Discov.* **3**, 578–589 (2013).
18. Kowanetz, M. et al. Granulocyte-colony stimulating factor promotes lung metastasis through mobilization of Ly6G+Ly6C+ granulocytes. *Proc. Natl Acad. Sci. USA* **107**, 21248–21255 (2010).
19. Perou, C. M. et al. Molecular portraits of human breast tumours. *Nature* **406**, 747–752 (2000).
20. Verhaak, R. G. W. et al. Integrated genomic analysis identifies clinically relevant subtypes of glioblastoma characterized by abnormalities in PDGFRA, IDH1, EGFR, and NF1. *Cancer Cell* **17**, 98–110 (2010).
21. Lehmann, B. D. B. et al. Identification of human triple-negative breast cancer subtypes and preclinical models for selection of targeted therapies. *J. Clin. Invest.* **121**, 2750–2767 (2011).
22. Carey, L. A. et al. Race, breast cancer subtypes, and survival in the carolina breast cancer study. *JAMA* **295**, 2492 (2006).
23. Nguyen, P. L. et al. Breast cancer subtype approximated by estrogen receptor, progesterone receptor, and HER-2 is associated with local and distant recurrence after breast-conserving therapy. *J. Clin. Oncol.* **26**, 2373–2378 (2008).
24. Kennecke, H. et al. Metastatic behavior of breast cancer subtypes. *J. Clin. Oncol.* **28**, 3271–3277 (2010).
25. Smid, M. et al. Subtypes of breast cancer show preferential site of relapse. *Cancer Res.* **68**, 3108–3114 (2008).
26. Gentles, A. J. et al. The prognostic landscape of genes and infiltrating immune cells across human cancers. *Nat. Med.* **21**, 938–945 (2015).
27. Li, B. et al. Comprehensive analyses of tumor immunity: implications for cancer immunotherapy. *Genome Biol.* **17**, 174 (2016).
28. Iglesia, M. D. et al. Prognostic B-cell signatures using mRNA-seq in patients with subtype-specific breast and ovarian cancer. *Clin. Cancer Res.* **20**, 3818–3829 (2014).
29. Iglesia, M. D. et al. Genomic analysis of immune cell infiltrates across 11 tumor types. *J. Natl Cancer Inst.* **108**, djw144 (2016).
30. Nagalla, S. et al. Interactions between immunity, proliferation and molecular subtype in breast cancer prognosis. *Genome Biol.* **14**, R34 (2013).
31. Maglione, J. E. et al. Transgenic polyoma middle-T mice model premalignant mammary disease. *Cancer Res.* **61**, 8298–8305 (2001).
32. Herschkowitz, J. I. et al. Comparative oncogenomics identifies breast tumors enriched in functional tumor-initiating cells. *Proc. Natl Acad. Sci. USA* **109**, 2778–2783 (2012).
33. Welte, T. et al. Oncogenic mTOR signalling recruits myeloid-derived suppressor cells to promote tumour initiation. *Nat. Cell Biol.* **18**, 632–644 (2016).
34. Tian, L. et al. Mutual regulation of tumour vessel normalization and immunostimulatory reprogramming. *Nature* **544**, 250–254 (2017).
35. Pfefferle, A. D. et al. Genomic profiling of murine mammary tumors identifies potential personalized drug targets for p53-deficient mammary cancers. *Dis. Model. Mech.* **9**, 749–757 (2016).
36. Gautier, E. L. et al. Gene-expression profiles and transcriptional regulatory pathways that underlie the identity and diversity of mouse tissue macrophages. *Nat. Immunol.* **13**, 1118–1128 (2012).
37. Bronte, V. et al. Recommendations for myeloid-derived suppressor cell nomenclature and characterization standards. *Nat. Commun.* **7**, 12150 (2016).
38. Coffelt, S. B. et al. IL-17-producing  $\gamma\delta$  T cells and neutrophils conspire to promote breast cancer metastasis. *Nature* **522**, 345–348 (2015).
39. Casbon, A.-J. et al. Invasive breast cancer reprograms early myeloid differentiation in the bone marrow to generate immunosuppressive neutrophils. *Proc. Natl Acad. Sci. USA* **112**, E566–E575 (2015).
40. Hanahan, D. & Coussens, L. M. Accessories to the crime: functions of cells recruited to the tumor microenvironment. *Cancer Cell* **21**, 309–322 (2012).
41. Kusmartsev, S. & Gabrilovich, D. I. Role of immature myeloid cells in mechanisms of immune evasion in cancer. *Cancer Immunol. Immunother.* **55**, 237–245 (2006).
42. Mabbott, N. A., Baillie, J. K., Brown, H., Freeman, T. C. & Hume, D. A. An expression atlas of human primary cells: inference of gene function from coexpression networks. *Genomics* **14**, 632 (2013).
43. Papayannopoulos, V., Metzler, K. D., Hakkim, A. & Zychlinsky, A. Neutrophil elastase and myeloperoxidase regulate the formation of neutrophil extracellular traps. *J. Cell Biol.* **191**, 677–691 (2010).
44. Semerad, C. L., Liu, F., Gregory, A. D., Stumpf, K. & Link, D. C. G-CSF is an essential regulator of neutrophil trafficking from the bone marrow to the blood. *Immunity* **17**, 413–423 (2002).
45. Newman, A. M. et al. Robust enumeration of cell subsets from tissue expression profiles. *Nat. Meth.* **12**, 453–457 (2015).
46. Curtis, C. et al. The genomic and transcriptomic architecture of 2,000 breast tumours reveals novel subgroups. *Nature* **486**, 346–352 (2012).
47. Ali, H. R., Chlon, L., Pharoah, P. D. P., Markowitz, F. & Caldas, C. Patterns of immune infiltration in breast cancer and their clinical implications: a gene-expression-based retrospective study. *PLoS Med.* **13**, e1002194 (2016).
48. Du, Z. et al. Introduction of oncogenes into mammary glands in vivo with an avian retroviral vector initiates and promotes carcinogenesis in mouse models. *Proc. Natl Acad. Sci. USA* **103**, 17396–17401 (2006).
49. Dyer, D. P. et al. TSG-6 Inhibits neutrophil migration via direct interaction with the chemokine CXCL8. *J. Immunol.* **192**, 2177–2185 (2014).
50. Korpala, M., Lee, E. S., Hu, G. & Kang, Y. The miR-200 family inhibits epithelial-mesenchymal transition and cancer cell migration by direct targeting of E-cadherin transcriptional repressors ZEB1 and ZEB2. *J. Biol. Chem.* **283**, 14910–14914 (2008).
51. Gregory, P. A. et al. The miR-200 family and miR-205 regulate epithelial to mesenchymal transition by targeting ZEB1 and SIP1. *Nat. Cell Biol.* **10**, 593–601 (2008).
52. Burk, U. et al. A reciprocal repression between ZEB1 and members of the miR-200 family promotes EMT and invasion in cancer cells. *EMBO Rep.* **9**, 582–589 (2008).
53. Toneff, M. J. et al. The Z-cad dual fluorescent sensor detects dynamic changes between the epithelial and mesenchymal cellular states. *BMC Biol.* **14**, 47 (2016).
54. Hännelmann, S., Castelo, R. & Guinney, J. GSVA: gene set variation analysis for microarray and RNA-Seq data. *BMC Bioinformatics* **14**, 7 (2013).
55. Taube, J. H. et al. Core epithelial-to-mesenchymal transition interactome gene-expression signature is associated with claudin-low and metaplastic breast cancer subtypes. *Proc. Natl Acad. Sci. USA* **107**, 15449–15454 (2010).
56. Subramanian, A. et al. Gene set enrichment analysis: a knowledge-based approach for interpreting genome-wide expression profiles. *Proc. Natl Acad. Sci. USA* **102**, 15545–15550 (2005).
57. Kaneda, M. M. et al. PI3K $\gamma$ 3 is a molecular switch that controls immune suppression. *Nature* **539**, 437–442 (2016).
58. De Henau, O. et al. Overcoming resistance to checkpoint blockade therapy by targeting PI3K $\gamma$  in myeloid cells. *Nature* **539**, 443–447 (2016).
59. Fridlender, Z. G. et al. Transcriptomic analysis comparing tumor-associated neutrophils with granulocytic myeloid-derived suppressor cells and normal neutrophils. *PLoS One* **7**, e31524 (2012).
60. Condamine, T. & Gabrilovich, D. I. Molecular mechanisms regulating myeloid-derived suppressor cell differentiation and function. *Trends Immunol.* **32**, 19–25 (2011).
61. Gabrilovich, D. I., Ostrand-Rosenberg, S. & Bronte, V. Coordinated regulation of myeloid cells by tumours. *Nat. Rev. Immunol.* **12**, 253–268 (2012).
62. Deaglio, S. et al. Adenosine generation catalyzed by CD39 and CD73 expressed on regulatory T cells mediates immune suppression. *J. Exp. Med.* **204**, 1257–1265 (2007).
63. Sitkovsky, M. & Lukashev, D. Regulation of immune cells by local-tissue oxygen tension: HIF1 alpha and adenosine receptors. *Nat. Rev. Immunol.* **5**, 712–721 (2005).
64. Netherby, C. S. & Abrams, S. I. Mechanisms overseeing myeloid-derived suppressor cell production in neoplastic disease. *Cancer Immunol. Immunother.* **66**, 989–996 (2017).
65. Maruyama, K. et al. The transcription factor Jdp2 controls bone homeostasis and antibacterial immunity by regulating osteoclast and neutrophil differentiation. *Immunity* **37**, 1024–1036 (2012).
66. Riaz, N. et al. Tumor and microenvironment evolution during immunotherapy with nivolumab. *Cell* **171**, 934–949.e15 (2017).
67. Hugo, W. et al. Genomic and transcriptomic features of response to anti-PD-1 therapy in metastatic melanoma. *Cell* **165**, 35–44 (2016).
68. Pahlter, J. C. et al. Plasticity in tumor-promoting inflammation: impairment of macrophage recruitment evokes a compensatory neutrophil response. *Neoplasia* **10**, 329–339 (2008).
69. Dongre, A. et al. Epithelial-to-mesenchymal transition contributes to immunosuppression in breast carcinomas. *Cancer Res.* **77**, 3982–3989 (2017).
70. Lou, Y. et al. Epithelial-mesenchymal transition is associated with a distinct tumor microenvironment including elevation of inflammatory signals and multiple immune checkpoints in lung adenocarcinoma. *Clin. Cancer Res.* **22**, 3630–3642 (2016).
71. Wellenstein, M. D. et al. Loss of p53 triggers WNT-dependent systemic inflammation to drive breast cancer metastasis. *Nature* <https://doi.org/10.1038/s41586-019-1450-6> (2019).

## Acknowledgements

We thank D. Weiss for critically editing the manuscript, and A. Muscarella, S. Kurley, S. Kim, J. Kim, B. Ton, L. Ma and S. I. Abrams for providing various tumour models. X.H.-E.Z. is supported by Breast Cancer Research Foundation, NCI CA151293, US Department of Defense DAMD W81XWH-16-1-0073 and W81XWH-18-1-0574, Susan G. Komen CCR14298445, and McNair Medical Institute. J.M.R. is supported by NCI-CA16303. Flow cytometry and cell sorting was performed at the Cytometry and Cell Sorting Core at Baylor College of Medicine with funding from the NIH (P30 AI036211, P30 CA125123 and S10 RR024574) and the expert assistance of J. M. Sederstrom.

**Author contributions**

Conception and design: X.H.-F.Z., I.S.K. and J.M.R. Development of methodology: I.S.K., X.H.-F.Z., T.W., M.J.T., H.W., J.L., K.S., Y.L., Q.M., T.F.W., C.Z., A.R., and A.S. Acquisition of data: I.S.K., Y.G., T.W., M.J., N.Z., A.G., Y.N., H.-C.L., I.B., T.N., W.B., W.J., J.A., F.G., J.H., D.J., K.W., and X.H.-F.Z. Analysis and interpretation of data: I.S.K., X.H.-F.Z., and J.M.R. Writing and review of manuscript: X.H.-F.Z., I.S.K., and J.M.R. Study supervision: X.H.-F.Z.

**Competing interests**

The authors declare no competing interests.

**Additional information**

**Supplementary information** is available for this paper at <https://doi.org/10.1038/s41556-019-0373-7>.

**Reprints and permissions information** is available at [www.nature.com/reprints](http://www.nature.com/reprints).

**Correspondence and requests for materials** should be addressed to X.H.-F.Z.

**Publisher's note:** Springer Nature remains neutral with regard to jurisdictional claims in published maps and institutional affiliations.

© The Author(s), under exclusive licence to Springer Nature Limited 2019

## Methods

**Mice.** All animal experiments were conducted in accordance with a protocol approved by Institutional Animal Care and Use Committee of Baylor College of Medicine. The study is compliant with all relevant ethical regulations regarding animal research.

Female animals of 6–8 weeks of age were used as the recipients of tumour tissue or cell line transplantation. Age-matched mice (10–12 weeks old) were subjected to euthanasia for immune profiling in all experiments. BALB/cAnNHsd (BALB/c), C57BL/6NHsd (C57BL/6 or B6), FVB and C.B-17/lcrHsd-Prkdc<sup>scid</sup>Lyst<sup>be-1</sup> (SCID/Beige) mice were purchased from Envigo and either directly used for experiments or bred in our facilities. B6.129S4-Ccr2<sup>tm1b6/j</sup> (CCR2-KO), B6.FVB-Tg(MMTV-PyVT)634Mul/LelJ (MMTV-PyMT), B6.Cg-Foxp3<sup>tm2Tch/j</sup> (B6.FOXP3-GFP), C.Cg-Foxp3<sup>tm2Tch/j</sup> (BALB/c.FOXP3-GFP) and C57BL/6J (WT) mice were purchased from The Jackson Laboratory and bred in our facilities. To generate CCR2-KO mice in a BALB/c background, CCR2-KO mice were crossed with WT BALB/c mice for five generations.

**Breast tumour models and transplantation.** Primary tumour tissue lines were maintained by implanting 1–2 mm<sup>3</sup> tumour pieces and cryopreserving following tumour harvest. Tumour models include T11 (BALB/c, p53-null tumour), 2208L (BALB/c, p53-null tumour), T1 (BALB/c, p53-null tumour), T12 (BALB/c, p53-null tumour), 2151R (BALB/c, p53-null tumour), 2245R (BALB/c, p53-null tumour), PyMT-M and -N (B6, MMTV-PyMT sub-lines), MMTV-WNT1 (FVB) and P53-PTEN DKO (FVB). The P53-PTEN DKO tumour tissue used for transplantation was derived from the MMTV-cre;Trp53<sup>F/F</sup>;Pten<sup>F/F</sup> strain, which was directly bred by J. Xu's lab at Baylor College of Medicine.

Cell lines were derived from above models and maintained as described in the 'Cell lines and cell culture' section. For inoculation into animals, cells were collected from culture with 0.25% trypsin (HyClone), washed with PBS (Lonza), counted, re-suspended in 1:1 solution of PBS and Matrigel (Pheno Red-free and growth factor reduced; BD Biosciences), and injected into the fourth mammary fat pad. Tumour models include (genetic background and cell numbers used for transplantation are indicated in parentheses): 4T1 (BALB/c, 0.5 × 10<sup>6</sup> cells), 4T07 (BALB/c, 1 × 10<sup>6</sup> cells), 67NR (BALB/c, 1 × 10<sup>6</sup> cells), T11 (BALB/c, 0.5 × 10<sup>6</sup> cells), AT3 (B6, 0.5 × 10<sup>6</sup> cells), E0771 (B6, 0.5 × 10<sup>6</sup> cells), E0771-ICBR (B6, 0.5 × 10<sup>6</sup> cells), PyMT-M and PyMT-N (B6, 0.5 × 10<sup>6</sup> cells) and PyMT-M-ICBR (B6, 0.5 × 10<sup>6</sup> cells).

PDXs were maintained by implanting 1–2 mm<sup>3</sup> tumour pieces into fat-pad-cleared mammary glands of SCID/Beige mice. The development of PDX lines was conducted under protocols approved by the Institutional Review Board. The current study used established PDXs that had been de-identified, and therefore has been granted protocol exemption by the Institutional Review Board for not involving human subjects.

Mammary fat pad transplantation and injection were performed using the same procedures as our previous studies<sup>33,34</sup>.

**Cell lines and cell culture.** All cell lines were cultured in DMEM/high glucose medium (HyClone), except E0771 (both parental and ICBR; CH3 Biosystems), which was cultured in RPMI-1640 medium (HyClone, supplemented with 10 mmol l<sup>-1</sup> HEPES (Gibco)). All media contained 10% FBS, 100 U ml<sup>-1</sup> penicillin, 100 µg ml<sup>-1</sup> streptomycin (Lonza) and 250 ng ml<sup>-1</sup> amphotericin B (Lonza), except that for 67NR, which was further supplemented with NEAA (Life technologies, cat. no. 11140050). All cells were grown in a humidified incubator at 37 °C, with 5% CO<sub>2</sub>. More information about cell lines can be found in the 'Eukaryotic cell line' section of the Reporting Summary.

**Human TNBC tissues.** The TNBC NanoString dataset ( $n=72$ ) was collected under a protocol approved by the Institutional Review Board at Scott and White Medical Center, Baylor Scott and White Healthcare. Informed consent from all participants were obtained. The other human datasets are all de-identified and obtained from publicly available sources (for example, TCGA), which were collected under protocols approved by the Institutional Review Board at the authors' institutions. The study is compliant with all relevant ethical regulations regarding research involving human participants. Raw macrophage counts (CD68<sup>+</sup>) for IHC staining (Fig. 2b,c) are provided in the far-right column of Supplementary Table 2c. In Fig. 2d, a continuous score of each tumour was computed by  $\Sigma \log_2(\text{MSG}_i)$ , in which MSG<sub>*i*</sub> represents individual macrophage-specific genes. These scores were compared against quantitative IHC scores of CD68. Since a large proportion of specimens on TMA were scored 0 and the rest of the data were sparsely distributed across a large range, we treated IHC scores as a categorical variable and used 10 as a cutoff to define two groups: negative/weak (<10) or strong (>10).

**miR-200c induction *in vitro* and *in vivo*.** T11, PyMT-M, E0771 and MDA-MB-231 cells were transduced with the doxycycline-inducible miR200c overexpression vector pINDUCER13-pre-miR-200c/141 (p13-miR-200/141) and selected for at least 3 days in 2 µg ml<sup>-1</sup> puromycin. T11 and MDA-MB-231 cell lines were also transduced with the Z-Cad sensor<sup>33</sup> that can identify carcinoma cells with EMT or MET properties, respectively. To induce miR-200c/141 *in vitro*, cells

were treated with doxycycline (DOX) (Sigma) for 1–2 weeks: 2 µg ml<sup>-1</sup> for T11 and PyMT-M, 500 ng ml<sup>-1</sup> for E0771, and 100 ng ml<sup>-1</sup> for MDA-MB-231. To induce miR-200c/141 *in vivo*, cells were first treated with 2 µg ml<sup>-1</sup> DOX for 2 weeks *in vitro* prior to inoculation to mice. DOX was administered to animals from day 1 post-tumour implantation until tumour harvest (2 weeks). Harvested tumours were immune profiled as well as re-transplanted to another batch of mice for further DOX induction (another 2 weeks) and immune profiling. Data were combined and analysed from both batches. A DOX solution of 1 mg ml<sup>-1</sup> was freshly prepared once a week, using 5% sucrose in water as the vehicle.

**Lentivirus transduction of tumour cells.** T11 cells were transduced with mouse ZEB1-specific shRNA (5'-ATATGTGAGCTATAGGAGC-3') or a scramble-control non-specific shRNA using the lentiviral pGIPZ vector system that allows puromycin selection to obtain pure transduced cell population.

***In vivo* drug treatment for immune checkpoint blockade and combination therapy.** On day 0 of experiments, tumour tissue pieces or cell lines were implanted orthotopically as specified in the previous section. Animals were randomized when tumours reached a similar size (4–5 mm in diameter, which was day 5–7 for cell line injection (4T1, AT3, E0771-Parental and -ICBR)) and given treatments with the following regimen for each drug. To size-match tumours, MMTV-Wnt1 tumour-bearing animals received initial treatment at various time points following transplantation due to variable tumour latency. 67NR was not included for this analysis due to its distinct growth kinetics, which makes it difficult to compare to all other models with regards to therapeutic response.

In Fig. 7a, 100 µg anti-CTLA4 (clone 9D9) and 200 µg anti-PD1 (clone RMP1-14) antibody were delivered every three days until the end-point (a total of 4–6 doses). In Supplementary Fig. 7a, treatment was initiated on day 1 post-tumour implantation and continued every other day until the end-point.

In Fig. 7b and Supplementary Fig. 7b,f, on day 0 of the experiment, 0.5 × 10<sup>6</sup> cells of the T11 tissue-derived cell line, E0771 cell line, PyMT-M and PyMT-N tissue-derived cell lines were inoculated orthotopically and randomized on day 5 for treatment initiation. ICB treatment was given every three days with the same dosage as described above (a total of 8 doses for T11, 4 doses for E0771, PyMT-M and PyMT-N).

In Fig. 8d, for the first 4 doses animals were given 100 µg anti-Ly6G (clone 1A8) every three days together with ICB (same dosage as described above), and for the next 8 doses given 200 µg anti-Ly6G without ICB every three days.

In Fig. 6d and Supplementary Fig. 7g, 100 µg (5 mg kg<sup>-1</sup>) of anti-Ly6G (clone 1A8) and 200 µg (10 mg kg<sup>-1</sup>) of CXCR2 inhibitor (Selleckchem, SB225002) were administered intraperitoneally every three days from tumour palpation until the end-point. ICB treatment was given every three days with the same dosage as described above. SB225002 was dissolved in DMSO and with 30% PEG300 (Sigma), 5% Tween 80 (Sigma) in distilled water.

In Fig. 5f, 0.5 mg of anti-CSF1 (clone 5A1) and 100 µl of clodrosome (Encapsula Nanosciences) were delivered through intraperitoneal and intravenous (retro-orbital) injection respectively and administered every five days, with different treatments spaced out by two to three days. Treatment was initiated on day 2 post-tumour transplantation for T11, PyMT-N and 2208L, and following tumour palpation for PyMT-M, and continued until the end-point (a total of 3–6 doses).

Control animals received an equal amount of isotype-matched antibodies (mouse IgG2b (clone MPC-11), rat IgG2a (clone 2A3) and rat IgG1 (clone HRPN)). All antibodies were delivered intraperitoneally and were purchased from BioXcell. Tumours were measured with a caliper and the volume was calculated using the formula  $\pi/6 \times \text{width}^2 \times \text{length}$ .

**Spontaneous pulmonary metastasis assay.** The assay was performed using eight tumour models implanted as either tissues or cell lines (10<sup>5</sup>–2 × 10<sup>5</sup> cells in 100 µl PBS) by orthotopic transplantation to mammary fat pads, followed by tumour resection when tumours reached ~1 cm<sup>3</sup>. The mice were closely monitored for one of the following end-points: (1) recurrent tumours reaching 2 cm<sup>3</sup>; (2) significant signs of morbidity; or (3) four months after resection. Lungs were extracted for examination of macroscopic metastases as previously described<sup>34</sup>.

**Tissue harvest and dissociation.** Tumours were resected when they reached approximately the size of 1 gram. For RNA-seq and immune cell profiling, orthotopic breast tumours were collected in ice-cold PBS and subjected to dissociation using the mouse Tumour Dissociation Kit (Miltenyi Biotec) according to the manufacturer's protocol. Tumours (0.2–0.4 g) were cut into small pieces (around 1 mm<sup>3</sup>) and transferred to gentleMACS C tubes (Miltenyi) containing 2.35 ml of RPMI-1640, 100 µl of enzyme D, 50 µl of enzyme R and 25 µl of enzyme A. Tissues were mechanically dissociated on a gentle MACS dissociator (Miltenyi). Three consecutive 'm\_Lung\_02' programs were run on the dissociator, with 10 min shaking incubation at 37 °C in between each program run. The dissociation reaction was stopped with ice-cold RPMI-1640 and a single-cell suspension was obtained by filtering through a 70 µm cell strainer (Greiner Bio-One). The single-cell suspension was centrifuged for 5 min at 350g, re-suspended in 1 ml RBC lysis buffer (eBioscience), incubated on ice for 1 min, and washed with 10 ml FACS buffer (PBS containing 1% FBS). Samples with >90% cell viability were used for further analyses.

Blood was drawn and collected in 0.5 M EDTA-coated tubes. To separate plasma from blood cells, a 15 min centrifugation at 1,500g and 4 °C was performed. Whole bone marrow and splenic immune cells were isolated by crushing the respective organ, and a single-cell suspension was obtained by filtering through a 70-µm cell strainer. Erythrocytes were lysed with RBC lysis buffer (Tonbo, cat. no. TMB-4300-L100) by incubating on ice for 10 min, after which cells were washed with FACS buffer.

**Flow cytometry.** Single-cell suspension was prepared as described in the ‘Tissue harvest and dissociation’ section. Cells were incubated for 10 min on ice with FcR blocker (1:100, clone 2.4G2, Tonbo) in FACS buffer. Cells were subsequently stained with directly conjugated antibodies in FACS buffer for 25 min on ice in the dark, followed by two washes with FACS buffer. FOXP3<sup>+</sup> regulatory T cells were identified by endogenous GFP signal from reporter mice (B6.FOXP3-GFP, BALB/c.FOXP3-GFP). Stained cells were immediately analysed or fixed with 0.5% PFA in PBS. All data were acquired using BD LSR Fortessa or LSR II Analyzer, and analysed with Flow Jo v10.0. The absolute number of tumour-infiltrating immune cells (over total number of cells in single cell suspension) was determined by using the liquid counting beads (BD Biosciences). The following antibodies were used for FACS sorting as well as immune profiling:

Myeloid cell phenotyping panel 1: CD45-violetFluor450 (clone 30-F11, Tonbo), CD11b-APC-Cy7 (clone M1/70, Tonbo), Ly6G-PerCPcy5.5 (clone 1A8, Tonbo), Ly6C-PE-CF594 (clone AL-21, BD Biosciences), F4/80-BV605 (clone BM8, Biologend), I-A/I-E-BV510 (clone M5/114.15.2, Biologend), CD11c-AlexaFluor700 (clone N418, Biologend), CD64-APC (clone X54-5/7.1, Biologend), CD103-PE-Cy7 (clone 2E7, Biologend), PDL1-BV711 (clone MIH5, BD Biosciences) and DAPI (NucBlue Fixed Cell ReadyProbes Reagent).

Myeloid cell phenotyping panel 2: CD45-violetFluor450 (clone 30-F11, Tonbo), CD11b-APC (clone M1/70, Tonbo), Ly6G-PerCPcy5.5 (clone 1A8, Tonbo), Ly6C-BV711 (clone HK1.4, Biologend), F4/80-FITC (clone BM8, eBioscience), I-A/I-E-BV510 (clone M5/114.15.2, Biologend) and CCR2-PE (R&D systems).

Lymphoid cell phenotyping panel 1: CD45-violetFluor450 (clone 30-F11, Tonbo), B220-APC-Cy7 (clone RA3-6B2, Biologend), CD3e-PerCPcy5.5 (clone 145-2C11, Tonbo), CD4-APC (clone GK1.5, Tonbo), CD8-FITC (clone 53-6.7, Tonbo), CD25-BV510 (clone PC61, BD Biosciences), PD1-BV605 (clone 29F.1A12, Biologend), γδTCR-PE (clone GL3, Biologend) and DAPI (NucBlue Fixed Cell ReadyProbes Reagent).

**Cell sorting and library preparation for RNA-seq.** To obtain pure tumour-infiltrating neutrophils (TINs) and macrophages (TIMs), breast tumours were dissociated into single-cell suspension by the same method as described in the ‘Tissue harvest and dissociation’ section. FACS sorting was performed using the Aria Cell Sorter (BD Biosciences) to purify TINs (DAPI<sup>-</sup>CD45<sup>+</sup>CD11b<sup>+</sup>Ly6G<sup>+</sup>Ly6C<sup>med-low</sup>) and TIMs (DAPI<sup>-</sup>CD45<sup>+</sup>CD11b<sup>+</sup>Ly6G<sup>-</sup>Ly6C<sup>F4/80</sup>). Cells were directly sorted into TRIzol LS (Invitrogen) and kept at -80 °C until further processing. RNA was extracted using the Direct-Zol RNA microprep kit (Zymo Research).

Following RNA isolation, MATQ-seq was performed to amplify the whole transcriptome TINs and TIMs as previously described<sup>34</sup>. Regular RNA-seq was performed for cancer cells’ RNA. The paired-ended reads were mapped to the mouse genome (UCSC mm10) using STAR (<https://github.com/alexandobin/STAR>) with NCBI RefSeq genes as the reference.

**RNA isolation and quantitative real-time polymerase chain reaction.** We followed procedures described in our previous publication for RNA isolation and qPCR<sup>34</sup>. The primers are listed in Supplementary Table 4.

**In vitro trans-well migration assay.** Bone marrow immune cells were harvested immediately from euthanized 8-week-old naïve WT (BALB/c and B6) mice as described in the ‘Tissue harvest and dissociation’ section. Following RBC lysis, neutrophils were enriched by positive selection using biotinylated anti-mouse Ly6G (clone 1A8, Biologend) and Ly6C<sup>high</sup> monocytes were enriched by negative selection using biotinylated anti-mouse antibodies against B220, CD3e (BD Pharmingen, cat. no. 559971) and Ly6G (clone 1A8, Biologend) as per the protocol of the EasySep Mouse Biotin Positive Selection Kit (STEMCELL technologies). For the trans-well migration assay, tumour-conditioned medium (TCM) containing 0.2% FBS (cultured for 24 hours) was added to the bottom of a 24-well plate. 1 × 10<sup>6</sup> cells of either neutrophils or monocytes (in the same medium used to generate TCM) were added to the upper chamber of trans-well inserts: 3 µm pore size for neutrophils (Corning, cat. no. 3415) and 8 µm pore size for monocytes (Corning, cat. no. 3422). Cells were incubated at 37 °C for 2 hours (neutrophils) or 4 hours (monocytes), following which inserts were removed, and cells in the bottom well were harvested. Flow cytometry was used to quantify migrated cells using liquid counting beads as a reference (BD Biosciences).

**In vitro T cell proliferation (suppression) assay by co-culture with neutrophils and monocytes.** CD3<sup>+</sup> T cells of naïve BALB/c or C57BL/6 mice (6–8 weeks old) were enriched from the spleen by negative selection using biotinylated anti-mouse antibodies against B220, CD11b, Gr1 (BD Pharmingen, cat. no. 559971)

and CD11c (BD Pharmingen, cat. no. 553800) followed by magnetic separation using the EasySep Mouse Biotin Positive Selection Kit (STEMCELL Technologies). Bone marrow neutrophils and monocytes from either naïve or relevant tumour-bearing animals were harvested as described in the ‘In vitro trans-well migration assay’ section. Magnetically sorted CD3<sup>+</sup> T cells were labelled with CFSE (5 µM, Molecular Probes) as per the manufacturer’s instructions. T cells were cultured alone or admixed with neutrophils or monocytes (at a 1:3 ratio) in a 96-well plate. T cell activation was with anti-CD3e (eBioscience, cat. no. 16-0031-85) through coating of wells overnight at 5 µg ml<sup>-1</sup>, 4 °C, and IL-2 (R&D, cat. no. 202-IL-010/CF) at 5 ng ml<sup>-1</sup>. After 4 days of co-culture, cells were collected and analysed for CFSE intensity by flow cytometry. Collected cells were also stained for Gr1-PE (eBioscience, cat. no. 12-5931-82) to be able to exclude non-T cells from the analysis. Proliferation index (%) was calculated as follows: (percentage of proliferated, co-cultured CD3<sup>+</sup> T cells)/(percentage of proliferated CD3<sup>+</sup> T cells cultured alone) × 100.

**Immunofluorescence and immunohistochemistry staining.** Tumour samples were fixed for one day (4 °C) with 10% neutral buffered formalin in PBS, incubated for one day (4 °C) in 30% sucrose, and subsequently frozen in optimal cutting temperature compound. Frozen sections were permeabilized with 0.25% Triton X-100 for 10 min at room temperature. After blocking for 1 hour at room temperature in blocking buffer (5% goat serum, 5% donkey serum, 2% BSA in PBS-GT), slides were incubated overnight in a humidified chamber at 4 °C with rat anti-mouse Ly6G (1:400, Tonbo, cat. no. 40-1276-U100) and rabbit anti-mouse CD68 (1:400, Abcam, cat. no. 125212). Slides were incubated with Alexa Fluor 594-conjugated goat anti-rabbit and Alexa Fluor 488-conjugated donkey anti-rat secondary antibody (1:250, Jackson ImmunoResearch) for 1 hour at room temperature. Slides were subsequently stained with SlowFade Gold antifade reagent with DAPI (Life Technologies, cat. no. S36936). Washing was performed in PBS between all steps. 10× and 40× images were taken with a Leica DMi8 microscope with a DMC4500 camera.

Tumour samples were fixed in 10% neutral buffered formalin and then paraffin-embedded. Microtome sectioning and immunohistochemistry staining was performed by the BCM Breast Center Pathology Core. Briefly, 3–4 µm thick sections were deparaffinized in xylene and graded alcohols, and treated with a heat-induced antigen retrieval buffer Tris-HCl 9.0 in a pressure cooker. Slides were blocked in 3% hydrogen peroxide solution for 5 min at room temperature. Primary antibodies were incubated for 1 hour at room temperature in antibody diluent solution (1% BSA in TBS-20) and subsequently stained with Envision Labelled Polymer-HRP anti-rabbit (Dako) for 30 min at room temperature. Slides were incubated with DAB<sup>+</sup> solution (DakoCytomation) for 15 min at room temperature, and with DAB Sparkle Enhancer (Biocare) to enhance the chromogen signal. Counterstaining in Harris Hematoxylin was performed and a coverslip was mounted. Washing was performed in TBS-20 between all steps. Primary antibodies include: oestrogen receptor (Santa Cruz, sc-542, 1:800), progesterone receptor (Dako, A0098, 1:100), ErbB2 (NeoMarkers, RB-103-P, 1:400), cleaved caspase 3 (Cell Signaling, 9661, 1:50), Ki67 (Cell Signaling, 122025, 1:400) and CD31 (Abcam, AB-124435, 1:400). Immunohistochemical images were obtained using an Olympus BX50F4 microscope and cellSens. All pictures are representative of at least three biological replicates in each group.

**Cell morphology analysis.** Cancer cell images were captured at a magnification of 10× using a Leica confocal microscope. 50,000 FACS-purified neutrophils (CD45<sup>+</sup>CD11b<sup>+</sup>Ly6G<sup>+</sup>Ly6C<sup>med-low</sup>) and macrophages (CD45<sup>+</sup>CD11b<sup>+</sup>Ly6G<sup>-</sup>Ly6C<sup>F4/80</sup>) were cyto-spun and dried slides were stained with Wright-Giemsa Stain (Sigma-Aldrich). Images were obtained at a magnification of 40× using a Leica DMLB microscope.

**Bioinformatics analyses.** Characterization of the eight syngeneic murine tumour models. RNA-seq was performed on the eight cell line models in technical triplicates as shown in Supplementary Fig. 1a. Genes corresponding to different properties of these cells were used for (1) TNBC heterogeneity (Supplementary Fig. 1d), (2) cytokine expression (Fig. 3f), and (3) EMT states (Fig. 4b). In particular, in Supplementary Fig. 1d, PyMT-N expresses GATA3, K8 and K18, whereas PyMT-M expresses vimentin, Zeb1 and Snail, suggesting that the two models represent luminal-like and claudin-low TNBC models, respectively.

**NanoString datasets.** Formalin-fixed paraffin-embedded (FFPE) tissue was first examined with hematoxylin and eosin staining to localize invasive tumour cells and surrounding area. A Roche High Pure FFPE RNA Isolation Kit was then used to purify RNAs. Macrodissection was performed when needed. Approximately 50 ng of total RNA was used to measure the expression of 730 immune-related genes and 40 housekeeping genes using the nCounter platform (NanoString Technologies) and the PanCancer Immune Profiling Panel. Data were log<sub>2</sub>-transformed and normalized using housekeeping genes selected using the nSolver 2.6 package. The normalized data are provided in Supplementary Table 2c.

**Derivation of macrophage-specific and neutrophil-specific genes for analysis of TNBC NanoString data.** Over 700 gene expression profiles of a variety of human cell types were obtained from Primary Cell Atlas of BioGPS (<http://biogps.org/>)

dataset/BDS\_00013/primary-cell-atlas/). All macrophage-based (regardless of conditions and treatments) were grouped and subjected to two comparisons: (1) to all other cell types, and (2) specifically to all neutrophil-based transcriptomic data. A statistical analysis of microarray (SAM) algorithm was employed for the comparisons and implemented by the 'siggenes' package of R. A cutoff of fold change (FC) >16 and FDR <0.1 were used for first comparison, and FC >8 and FDR <0.1 were used for the second comparison. Genes selected by both comparisons were used as MSGs. The same procedures and cutoffs were applied to identify NSG. Specific arrays used in comparisons are listed in Supplementary Table 2a. These genes were then intersected with genes contained in the nanostring TNBC dataset. 33 MSGs and 45 NSGs were identified, as listed in Supplementary Table 2b. Unsupervised hierarchical clustering was performed using the 'heatmap.2' function in the 'gplots' package of R. Ward clustering algorithm was used and the sample distance was defined by the Manhattan approach (absolute distance between two vectors). The resulted cluster structures were then superimposed with the expression of the CSF3, ELANE and CD68 genes, as well as IHC staining results of CD68 of the same dataset.

In Fig. 2d,  $\Sigma \log_2(\text{NSG}) - \Sigma \log_2(\text{MSG})$  was used to compute a single score for each tumour. The distribution of this score was examined as a histogram. The bimodal distribution was approximated by the 'normalmixEM' function in the 'mixtools' package of R.

**TIMER and CIBERSORT analysis of immune cell infiltration in RNA-seq/microarray datasets of bulk tumours.** We obtained RAN-seq profiles of breast cancer from TCGA data portal in June 2016. To avoid any potential batch effects, we only chose samples profiled at UNC and stored in a folder named 'RNASeqV2'. 1,073 profiles were collected. We then used associated IHC-determined ER/PR/ErB2 statuses to extract 112 triple-negative breast cancer samples. We did not perform any additional selection of samples. The barcodes or IDs of all samples included in our analyses are listed in Supplementary Table 2d.

TIMER output of TCGA tumour specimens was downloaded from the algorithm website (<https://cistrome.shinyapps.io/timer/>). Immune cell infiltration estimates of the corresponding 1,073 TCGA breast tumours were isolated by matching the barcodes and IDs. The distribution of all six types of immune cells across TNBC and non-TNBC is displayed in Fig. 2e and Supplementary Fig. 2a by using the 'heatmap.2' function with the option of 'Manhattan' of the distance function and the option of 'Ward.D2' of the 'hclust' function for dendrogram computation. The tSNE analyses (Fig. 2f and Supplementary Fig. 2b, c) were implemented by the 'tSne' package of R with perplexity = 10 and other parameters in default setting.

CIBERSORT output was downloaded from website provided in the reference<sup>47</sup>. TNBC tumours were isolated based on associated annotations and displayed by hierarchical clustering using 'heatmap.2' with the option of 'Manhattan' of the distance function and the option of 'Ward.D2' of the 'hclust' function for dendrogram computation. The predicted relative abundance of neutrophils and macrophages were also displayed as stacked bar graphs using the 'ggplot2' package of R in Fig. 2g.

In Fig. 4f and Supplementary Fig. 4h,i, GSEA was applied to the TCGA TNBC dataset, using TIM-TIMER scores and TIN-TIMER scores as continuous phenotypic values and hallmark pathway as gene sets. Pathways with  $P < 0.05$  and FDR <0.1 were selected and displayed in Fig. 4f. The graphic output depicting correlation between TIM and EMT and between TIN and PI3K-AKT-mTOR were shown in Supplementary Fig. 4h,i, respectively.

In Fig. 4g and Supplementary Fig. 4j, we applied gene set variation analysis (GSVA) to three hallmark pathways and an EMT signature defined previously<sup>55</sup>. GSVA was implemented using the 'gsva' package of R, and under default settings except for 'RNAseq = TRUE'. The EMT signature was obtained from the supplementary material of the original paper<sup>55</sup>, and contains 91 upregulated and 160 downregulated genes. There are 32 genes in common between the 91 upregulated genes and the 200 hallmark EMT genes. The correlation between TIMER scores and pathway GSVA scores were assessed by Pearson correlation coefficients (Supplementary Fig. 4j).

In Fig. 4h, miR-200c expression TCGA TNBC was obtained from the TCGA data portal and compared against TIM scores predicted by TIMER.

In Fig. 8f,h and Supplementary Fig. 8i, we analysed two datasets<sup>66,67</sup>. The normalized transcriptome profiles (regularized log-transformed) were uploaded to the TIMER website to generate estimates of immune cell infiltration, which are displayed as heatmap shown in Fig. 8f,h with samples ordered according to the TIN scores. Z-scores of TIN were compared between different therapy response groups in the first dataset<sup>66</sup> (Fig. 8g), in which only pre-treated tumours were included.

The distribution of TIN scores was examined by histogram (Supplementary Fig. 8h), which exhibited an asymmetric pattern with long right tail. Normality tests (Shapiro test and Skew test implemented in R) confirmed this observation. We then examined the Q-Q plot and noted that approximately 20% of points fall above the normality line (Supplementary Fig. 8g). Indeed, removal of the top 20%

tumours renders the rest following normal distribution (Supplementary Fig. 8h). Therefore, the top 20% was determined as a cutoff to define a distinct group of tumours with exceptionally high TINs (Supplementary Fig. 8i).

**Bioinformatics analysis of macrophage and neutrophil transcriptomes from different tumour models.** RNA-seq data of macrophages and neutrophils were analysed by GSVA for the 50 hallmark gene sets (<http://software.broadinstitute.org/gsea/msigdb/genesets.jsp?collection=H>), using the same tools described in previous section. The results are exhibited by hierarchical clustering in Figs. 5b and 6b. Principle component analysis (PCA) was used to analyse macrophage data shown in Fig. 5a, as implemented by the 'prcomp' package in R.

The pre-processed, quantile-normalized GSE43254 dataset was downloaded from GEO<sup>39</sup>. Genes that are differentially expressed between normal neutrophils versus gMDSCs or TANs were identified using SAM by criteria: FDR <0.1 and fold change >10. These genes are listed in Supplementary Table 3a, and were used to cluster the neutrophil profiles in our tumour models in an unsupervised fashion (Fig. 6a).

For GO-enrichment analyses, FDR <0.05 were used to define TIN-enriched genes. GOstats was then carried out to calculate GO terms enriched in up-regulated and down-regulated genes in neutrophils of NES tumours. We focused on GO terms that contain more than five genes,  $P < 0.001$  and odds ratio >3.250. Identified GO terms are listed in Supplementary Table 3b, seven of which are related to purine metabolism or signalling. To further test the hypothesis, we downloaded 86 gene sets from MSigDB that are related to adenosine or purine by searching these keywords. GSEA was then carried out using these gene sets. 25 gene sets were scored as significant using FDR <0.1 as a cutoff, and are listed in Supplementary Table 3c. Four representative pathways are shown in Supplementary Fig. 6b.

**Statistics and reproducibility.** Data were analysed with Microsoft Excel functions, Prism 7 software (GraphPad) or R programming language. Statistical analysis was performed using unpaired or paired two-tailed Student's *t*-test (with unequal variations if an F-test ruled out the equal variation assumption), ANOVA analysis, log-rank test (survival analysis), Fisher's exact test or Shapiro test, as appropriate for the dataset. Statistical details (for example, sample size and specific test performed) for each experiment are denoted in the corresponding figure or figure legends. Individual mouse and independent in vitro samples (independent batch experiments, different tumour models and different animals) were considered biological replicates. All biologically independent samples were included and combined for statistical analyses. Experimental findings were reliably reproduced. In each experiment, the group sizes were determined based on the results of preliminary experiments and no statistical method was used to predetermine sample size. Data are shown as means  $\pm$  standard deviation (s.d.) unless otherwise specified. In box and whisker plots, the middle line is plotted at the median, the upper and lower hinges correspond to the first and third quartiles, and the upper and lower whiskers extend no further than  $1.5 \times$  IQR from the hinges (IQR, interquartile range or distance between first and third quartiles). *P* values lower than 0.05 were considered statistically significant. The statistical source data are included in Supplementary Table 5.

**Reporting Summary.** Further information on research design is available in the Nature Research Reporting Summary linked to this article.

## Data availability

The RNA-seq data for cancer cells, tumour-infiltrating macrophages and tumour-infiltrating neutrophils have been submitted to the Gene Expression Omnibus under accession number GSE104765. The normalized RNA-seq data for human TNBC nanostring datasets are provided in Supplementary Table 2c.

Other secondary datasets used in this study include

1. TCGA dataset, available from <https://portal.gdc.cancer.gov/>. The sample IDs used in this study are provided in Supplementary Table 2d.
2. METABRIC dataset, available from <https://ega-archive.org/datasets/EGAD00010000266>.
3. BioGPS Primary Cell Atlas, available from [http://biogps.org/dataset/BDS\\_00013/primary-cell-atlas/](http://biogps.org/dataset/BDS_00013/primary-cell-atlas/). The specific samples used in this study are listed in Supplementary Table 2a.
4. Gene expression profiles of TAN, GMDSC and normal neutrophils. Data available from GEO, dataset GSE43254.
5. Metastatic melanoma dataset<sup>66</sup>: [https://github.com/riazn/bms038\\_analysis](https://github.com/riazn/bms038_analysis)
6. Metastatic melanoma dataset<sup>67</sup> available from GEO: GSE78220.

## Code availability

Key codes for data analyses and major intermediate data are available at Github: <https://github.com/Xiang-HF-Zhang/Dichotomous-of-innate-immune-landscape>.